TRACING THE EVOLUTIONARY HISTORY OF MASSIVE GALAXIES WITH GLOBULAR CLUSTERS

TRACING THE EVOLUTIONARY HISTORY OF MASSIVE GALAXIES WITH GLOBULAR CLUSTERS: A JWST NIRCAM PHOTOMETRIC STUDY OF GLOBULAR CLUSTER POPULATIONS IN INTERMEDIATE-REDSHIFT GALAXY CLUSTERS

By KAITLYN E. KEATLEY, B.Sc.

A Thesis Submitted to the School of Graduate Studies in Partial Fulfillment of the Requirements for the Degree Master of Science

McMaster University

MASTER OF SCIENCE (2025)

Hamilton, Ontario, Canada (Physics and Astronomy)

TITLE:	Tracing the evolutionary history of massive galaxies with globular clusters: A JWST NIRCam photometric study of globular cluster populations in intermediate-redshift galaxy clusters
AUTHOR:	Kaitlyn E. Keatley B.Sc. (Astrophysics), McMaster University, Hamilton, Canada
SUPERVISOR:	Dr. William E. Harris
NUMBER OF PAGES:	xiv, 72

Abstract

Massive, gravitationally bound star clusters, globular clusters (GCs) are among the oldest objects in the universe. Because they preferentially formed in the early universe, understanding their formation and evolution is challenging due to limited observational data. The James Webb Space Telescope (JWST) allows us to extend observations of GC populations to intermediate redshift; colour-magnitude diagrams (CMDs) and spatial distribution of GC populations can reveal the history of their host galaxies. By comparing CMDs of GC systems across epochs, we can further understand their evolution. These populations can also be used to probe the gravitational potential of massive galaxy clusters, which is dominated by the dark matter halo. This work focuses on the galaxy cluster RXJ 2129.5+0007 at a redshift of 0.234 (lookback time of 2.9 Gyr). We have conducted photometry utilizing three bands from the short wavelength channel of NIRCam (F115W, F150W, and F200W). We explore the CMD, radial and azimuthal distribution, and subpopulations of candidate GCs around the brightest cluster galaxy of RXJ 2129.

Acknowledgements

Firstly, thank you to my supervisor, Dr. Bill Harris. I couldn't ask for a better mentor. Your guidance, patience, and encouragement have shaped this work and helped me grow as a researcher.

I also thank the rest of my committee, Dr. Laura Parker and Dr. Chris Wilson, for your thoughtful input and support throughout this process.

To my officemates, Raven and Jinoo – thank you for your friendship through all the joys and rough patches that have come with this journey. You both have an incredible boldness that pushes me to charge forward. Aditi, thank you for being there no matter what. Drew, Bennett, Atesh, Levi, and Jing – thank you for making these years interesting and memorable.

I am so grateful to be a part of such a fantastic department. I have learned more in the past two years than I would've thought possible.

Table of Contents

List of Figures

List of Tables

Notation and Abbreviations

Notation

$\mathbf{m}_{F115W}$	Instrumental magnitude in the F115W filter, as returned by the *all-star* PYRAF function using a 3px-radius aperture.
F115W (magnitude)	Apparent magnitude in the F115W filter, AB mags
$\mathbf{F115W}_0$	Absolute magnitude in the F115W filter, AB mags
[Fe/H]	Metallicity, defined as the logarithmic ratio of the number of iron nuclei per proton
MJy/sr	MegaJanskys / steradian (unit)
nJy	NanoJanskys (unit)
$\mathbf{A}_\lambda$	Galactic extinction in filter λ
$\mathbf{k}_\lambda$	Cosmological K-correction in filter λ

Abbreviations

AMR	Age-metallicity relation
BCG	Brightest cluster galaxy
CMD	Colour-magnitude diagram
EEF	Encircled energy fraction
FWHM	Full width half maximum
GC	Globular cluster
GMC	Giant molecular cloud
ICL	Intracluster light
MDF	Metallicity distribution function
PSF	Point spread function
SED	Spectral energy distribution

Co-Authorship

I, Kaitlyn Keatley, declare the contents of this thesis titled *Tracing the Evolutionary History of Galaxy Clusters with Globular Clusters* are my own and the work presented is original. Chapter 2 contains work published in the refereed journal *The Astrophysical Journal* (ApJ). I carried out the data analysis, prepared figures, and wrote the text of the paper. This work was co-authored with my supervisor, Dr. William Harris.

Chapter 1

Introduction

1.1 Globular Clusters and their Formation

Globular clusters (GCs) are old, massive, compact star clusters. The majority of present-day GCs formed 10-13 Gyr ago (Leaman et al., 2013), which raises substantial observational challenges to understand their formation and evolution. Harris and Pudritz (1994) proposed that GCs, like all star clusters, form within giant molecular clouds (GMCs) (recent studies have proven this, including Choksi et al. (2018); Reina-Campos et al. (2022); Gieles et al. (2025); see Kruijssen (2025) for a review). GCs are the highest mass end of star formation, forming in extremely high pressure and turbulent clouds. Finding such conditions was commonplace in the early universe (Reina-Campos et al., 2019). As the universe expanded and average pressures and densities decreased, these conditions became more and more difficult to achieve, up to the present day universe where massive cluster formation is rare except in starbursts during major mergers.

Figure 1.1 illustrates how turbulence and inflows drive massive cluster formation.

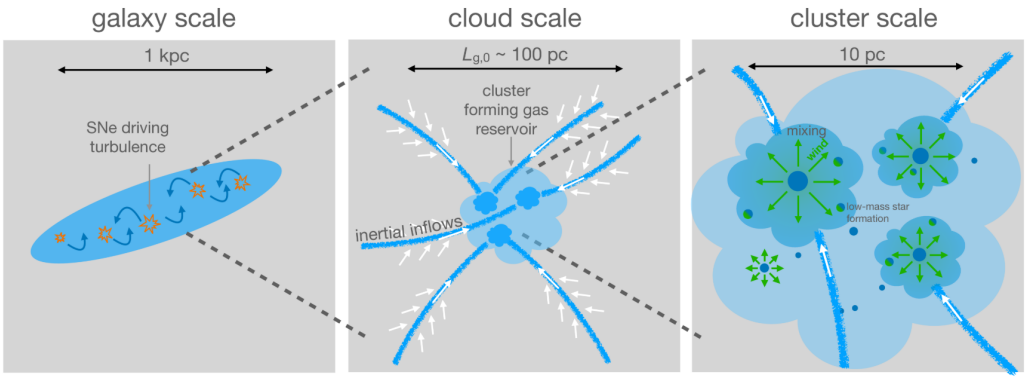

Figure 1.1: Schematic of proto-GC formation. Supernovae drive inflows on 100 pc scale, and clusters accumulate in the centre of the cloud with the gas reservoir. Figure from Gieles et al. (2025).

The conditions that birth young massive clusters are volatile and violent–unsuitable for a gravitationally bound cluster to survive. Shocks, supernovae, and tidal forces disrupt the majority of proto-GCs in their natal environment. In order for a massive cluster to survive and live to be a GC, it must be kicked out of the GMC (Kruijssen, 2012). There is a high interaction rate in this dense regime; other star clusters and gas clouds provide gravitational kicks over time. The strength of the tidal field decreases further from the dense central parts of the galaxy (Li and Gnedin, 2019), increasing the odds of survival for those clusters that are ejected into the halo. Simulations predict that 70-80% of proto-GCs are disrupted before $z = 0$, with more massive clusters having better chances of survival (Li and Gnedin, 2019; Chen and Gnedin, 2023b).

Even the surviving GCs have lost substantial mass throughout their long lives. Tidal effects, such as passing through a disky galaxy midplane, can slowly compound disruptions until the cluster becomes unbound. Stellar streams in the Milky Way give us some opportunity to study disrupted GCs, though this has its own challenges (see

Bonaca and Price-Whelan (2024) for a review on stellar streams).

The globular cluster luminosity function (GCLF) is a log-normal function with a characteristic turnover. The peak in this function, or the GCLF turnover, is nearly universal at $10^5 L_\odot$ with only a weak dependence on host galaxy mass (Harris et al., 2014). Recent models and simulations show that evolutionary processing plays a key role in establishing the observed GCLF, with low-mass clusters being progressively destroyed while surviving clusters gradually decrease in luminosity as their stellar populations age (Reina-Campos et al., 2022).

Through natal destruction and tidal disruption, the GCs we observe in the local universe today are a strictly limited sample of massive clusters that have formed. Simulations provide insights into the formation and evolution of GCs, but observations of GC systems at earlier times in their lives are necessary to test these theories.

1.2 Age-metallicity relation and subpopulations

Because all of a GC's stars are formed together, a single GC shows little-to-no spread in iron content. *Systems* of GCs in large galaxies, however, conventionally show a bimodal distribution in their optical colour, which is closely related to their metallicity (Fahrion et al., 2020). Zinn (1985) first observed this trend in the Milky Way GCs. This bimodality in the metallicity distribution function (MDF) has been observed in many systems since, notably M31 (Barmby et al., 2000; McConnachie et al., 2018), NGC 4472 (Strader et al., 2007), NGC 5128 (Woodley et al., 2010), NGC 4594 (Alves-Brito et al., 2011), NGC 3115 (Arnold et al., 2011), and M81 (Ma et al., 2013). Larger scale studies have also identified bimodality in the MDF (Peng et al., 2006; Foster et al., 2010; Caldwell and Romanowsky, 2016; Harris, 2023; Hartman et al., 2023).

This trend appears across a large range of galaxy masses, suggesting that galaxies of all sizes are subject to the same family of processes that drive GC formation and evolution (Peng et al., 2006).

The division of GCs into two populations hints at different origins of the clusters. GC metallicity is the strongest indicator of host galaxy mass at time of formation – simulations and observations show a wide range of GC metallicities at any age, reflecting a large range in progenitor masses (Kruijssen et al., 2018; Kruijssen et al., 2019; Chen and Gnedin, 2023b). Therefore, we may predict that more metal-rich GCs formed in massive galaxies, while metal-poor GCs formed in dwarf galaxies which were later accreted into larger systems. This is a generalization of a series of complex relationships that we can better understand using the age-metallicity relation (AMR). The AMR for GCs probes mass growth, metal enrichment, and minor merger history of the galaxy (Kruijssen et al., 2019). However, ages are highly uncertain for observations beyond the Local Group; confident age measurements rely on a colour-magnitude diagram (CMD) of resolved stars. Despite the limitations, we have learned much about GC subpopulations through study of AMRs. Leaman et al. (2013) found that the AMR of Milky Way disk GCs closely matches the AMR of the thin disk stars, while the AMR of halo GCs is in good agreement with dwarf galaxies with masses $M \sim 10^7 - 10^9 M_\odot$. The authors also found that the metal-rich subpopulation of Milky Way GCs *at any age* is more metal rich by ~ 0.6 dex in [Fe/H] than the metal-poor population (Leaman et al., 2013). Conversely, metal-rich clusters are systematically younger than metal-poor clusters by up to 3 Gyr (Li and Gnedin, 2019). This demonstrates that subpopulations of GCs date back to their formation. Interestingly, results from the E-MOSAICS simulations suggest that the GC MDF

is initially unimodal in most galaxies, and bimodality results from cluster disruption (Pfeffer et al., 2023). Complex processes shape these populations over time, and there are many open questions still to be explored.

Due to their differing origin, the subpopulations of GCs also differ in the shape of their spatial distribution. GCs accreted from small dwarfs have large galactocentric radii, while those belonging to more massive merging galaxies will preferentially sink to the centre of the accretor via dynamical friction (Leaman et al., 2013). On average, metal-poor subpopulations have shallower and more extended radial profiles than metal-rich GCs, as they are deposited in the halo by accreted satellite galaxies (Reina-Campos et al., 2022). In-situ GCs are naturally more centrally concentrated, though those that are ejected into the halo have a greater probability of survival.

To summarize the two subpopulations often exhibited by GC populations:

1. The more metal-poor population exhibit a trend of bluer colours, older ages, and have a roughly spherical distribution.

2. The more metal-rich GCs have redder colours, are younger, and are more centrally concentrated.

1.3 GC system - halo size relation

The distribution of a system of GCs is governed by the gravitational potential of the host galaxy or galaxy cluster. Many studies have observed a strong correlation between the number of GCs in a system and the host galaxy: its size, stellar mass, and mass of the dark matter halo (Blakeslee et al., 1997; Harris et al., 2017). This trend is also reproduced when considering the mass or the effective radius of the GC system

(Harris et al., 2015; Forbes et al., 2016; Hudson and Robison, 2018). This trend extends all the way from dwarf galaxies (Forbes et al., 2018) to the high-mass end of brightest cluster galaxies (BCGs) (Dornan and Harris, 2023; Dornan and Harris, 2025) – that's 6 orders of magnitude in host galaxy mass! The GC-halo relation is the same for all morphological types, suggesting that the amount of gas available at the time of GCs formation was nearly directly proportional to the dark matter halo potential (Harris et al., 2015; Choksi et al., 2018).

Giant ellipticals can host tens of thousands of GCs, while dwarf galaxies may have a handful, or none at all. A barren dwarf may have never been able to achieve gas surface densities high enough to form massive clusters, or its population may have been destroyed or ejected by tidal stripping (Forbes et al., 2018). Chen and Gnedin (2023a) found that most dwarf galaxies with stellar mass less than $2 \times 10^7 M_\odot$ do not host GCs.

The scarcity of GCs with metallicity below [Fe/H] $= -2.5$ across all systems suggests a minimum galaxy mass required to form long lived GCs (Kruijssen, 2019). Simulations predict that essentially all proto-GCs with initial mass lower than $10^5 M_\odot$ are disrupted by present day (Li and Gnedin, 2019; Reina-Campos et al., 2022), reiterating that local universe GCs represent only a small surviving sample of what was a much larger population at formation.

1.4 GCs as a dark matter probe

This leads us into the primary motivation of this work. Galaxies lie within massive, extended potential wells of dark matter. We have established that GC distribution correlates with mass; the dark matter halo dominates the gravitational potential field

of galaxies, and therefore GCs have great potential as probes of the halo. The work done by Reina-Campos et al. (2022) provides computational evidence using the E-MOSAICS simulations (MOdelling Star cluster population Assembly In Cosmological Simulations within EAGLE; Pfeffer et al. (2018); Kruijssen et al. (2019)); they found that the projected number density of GCs traces the density profile of dark matter. In order to observationally test this theory, we must compare GC spatial distributions to mass profiles of massive galaxies and galaxy clusters.

GCs are not the first candidate tracer of the dark matter halo; the distributions of satellite galaxies and the diffuse stellar halo are also governed by the gravitational field. Pillepich et al. (2017) and Alonso Asensio et al. (2020) found promising correlations between projected distributions of stellar haloes and dark matter halos in simulations, although with substantially different radial profiles. Observationally, the stellar halo becomes very difficult to measure at large radii, limiting its use as a tracer. Satellite galaxies have also been used to probe the gravitational field in the outskirts of galaxy clusters (Alabi et al., 2016; Slizewski et al., 2022); however, the kinematic models used to do this require very accurate spectroscopy. GCs are brighter and more extended than the diffuse stellar halo, and more numerous than satellite galaxies. GCs can be detected at large galactocentric radii, making them an extremely promising probe.

How do you model a mass profile when most of the mass is invisible? Luckily, while we may not understand what exactly dark matter *is*, we do have a pretty good understanding of how light interacts with it. Gravitational lensing is the process by which a very massive object bends light rays toward the viewer, allowing us to see things that in a Euclidean universe would never reach us. This has a wealth of

usages; most notable is the magnification of high-redshift star forming complexes and proto-GCs, such as the Sunrise Arc at $z \sim 6$ (Vanzella et al., 2023).

Pertinent to this work, another innovative use of gravitational lensing is to model the mass distribution of strong lensing galaxy clusters. Besides magnifying background galaxies, gravitational lensing can also produce multiple images of the same galaxy, which are identified with spectroscopy. Using the redshifts and positions of multiple images, we can model the mass of the galaxy cluster required to reproduce such images. This is illustrated in Figure 1.2. Lensing maps of clusters in the range $z = 0.2 - 0.5$ will allows us to compare total mass to GC distribution.

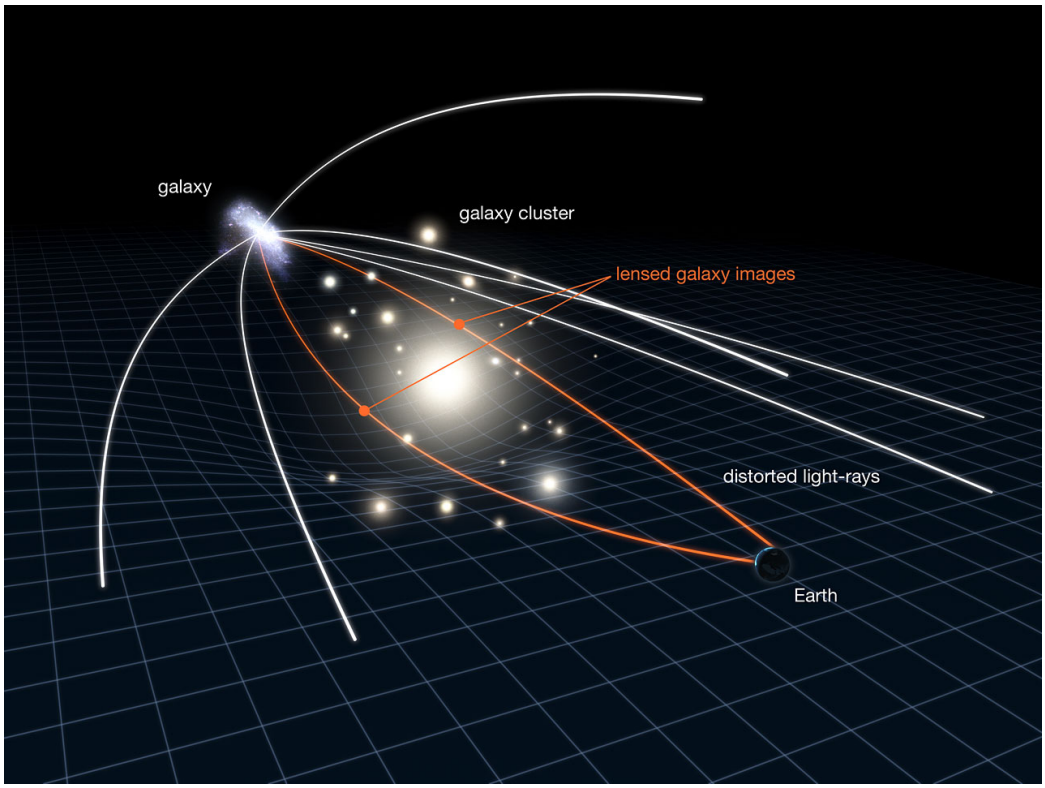

Figure 1.2: Schematic of how multiple images of background galaxies are produced by gravitational lensing in galaxy clusters. Image credit: NASA, ESA & L. Calçada.

1.5 A New Era of GC Observations

Part of what makes GCs so interesting to study are the challenges of doing so. They are incredibly small at intermediate redshift, requiring high resolution to resolve them. They are much dimmer than their host galaxies, requiring galaxy light to be carefully removed along with long exposure times to procure adequate depth. With the launch of JWST in 2022, the capabilities of direct GC observations have taken a massive leap.

JWST has a slightly better diffraction-limited resolution in the near-infrared than HST has in the optical bands, and a much larger light-collecting area. In Figure 1.3, we compare two zoom-ins on a BCG – an HST Wide Field Camera 3 (WFC3) image on the left and a JWST Near Infrared Camera (NIRCam) image on the right. The inverted images are median subtracted, meaning large scale light contours are removed to make it possible to detect point source GCs deep into the BCG light. GCs are visible in the JWST image as small dots, while GC detection in the HST image is laughable.

Direct observations of GC populations are no longer limited to the local universe. Intermediate redshift systems recently studied with JWST include SMACS J0723.3–7327 (Lee et al., 2022), VV 191a (Berkheimer et al., 2024), Abell 2744 (Harris and Reina-Campos, 2023; Harris and Reina-Campos, 2024), MACS J0416.1-2403 (Berkheimer et al., 2025), and MACS0417.5-1154 (Harris et al., in prep). JWST has smashed expectations with observations of GCs in El Gordo, a galaxy cluster at $z = 0.87$ and a lookback time of 7.36 Gyr. Since luminosity of GCs decreases over time, it works in our favour that more distant GCs also tend to be brighter! Despite the modest depth of the short-wavelength NIRCam images of El Gordo, Harris et al.

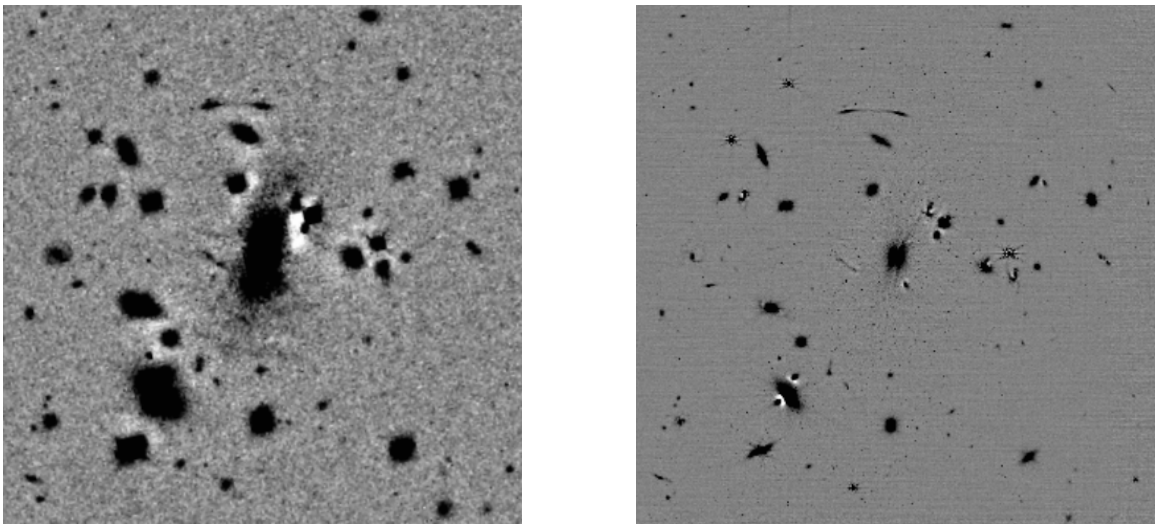

Figure 1.3: HST WFC3, F160W (left) and JWST NIRCam, F150W (right) images centered on the BCG of RXJ 2129. Both images are 48.9" x 48.9" and median-subtracted.

(2025) detected a sequence of candidate GCs well separated from the background galaxy field. This indicates that JWST should be capable of direct GC observations at $z = 1$, and likely up to $z \sim 1.4$ (Harris et al., 2025).

1.6 Intermediate redshift strong lensing galaxy clusters

Due to photometric constraints at intermediate-high redshift, studying GC populations in the early universe has only been possible on a case-by-case basis. Statistical studies of young GCs are currently non-existent. Despite these obstacles, every GC system that can be studied in depth adds to the slow and steady accumulation of knowledge about these fascinating systems.

The primary focus of this work is the massive galaxy cluster RXJ 2129.7+0005

(hereafter referred to as RXJ 2129). It sits at a redshift of 0.234 corresponding to a lookback time of 2.90 Gyr. A currently virialized cluster with one central BCG, RXJ 2129 has some major mergers in its history as revealed by an X-ray cold front in the intracluster light (ICL) (Jiménez-Teja et al., 2024). It has a mini radio halo around the BCG, and a strong cool core (Kale et al., 2015; Giacintucci et al., 2017; Ueda et al., 2020). Rines et al. (2013) calculated a halo mass of $5.59 \pm 1.16 \times 10^{14} M_{\odot}$ using X-ray flux by, while Umetsu et al. (2018) determined a mass of $7.8 \pm 2.4 \times 10^{14} M_{\odot}$. These values are in quite good agreement, corresponding to a virial radius around $r_{200} = 1.3$ Mpc.

The strong lensing features of RXJ 2129 have brought attention to this system; it was a target of the Cluster Lensing And Supernova survey with Hubble (CLASH, Postman et al. (2012)), leading to many strong and weak lensing studies on its mass distribution (Desprez et al. (2018); Umetsu et al. (2018); Caminha et al. (2019); Jauzac et al. (2021); Caminha et al. (2022)). Kelly et al. (2022) observed a high redshift triply lensed supernova, shown in Figure 1.4. The image that is formed by the longest light path (ie. looking the furthest back in time) displays the brilliant supernova at $z = 1.52$, while it has faded in the later two images. RXJ 2129 is a complex system whose GC system has not previously been studied.

1.7 Outline of This Thesis

In this thesis, I conduct an in-depth photometric analysis of the GC population of RXJ 2129. This work contributes to the accumulation of studies of GC populations in galaxy clusters at intermediate redshift, which is possible with the recent advancements of JWST.

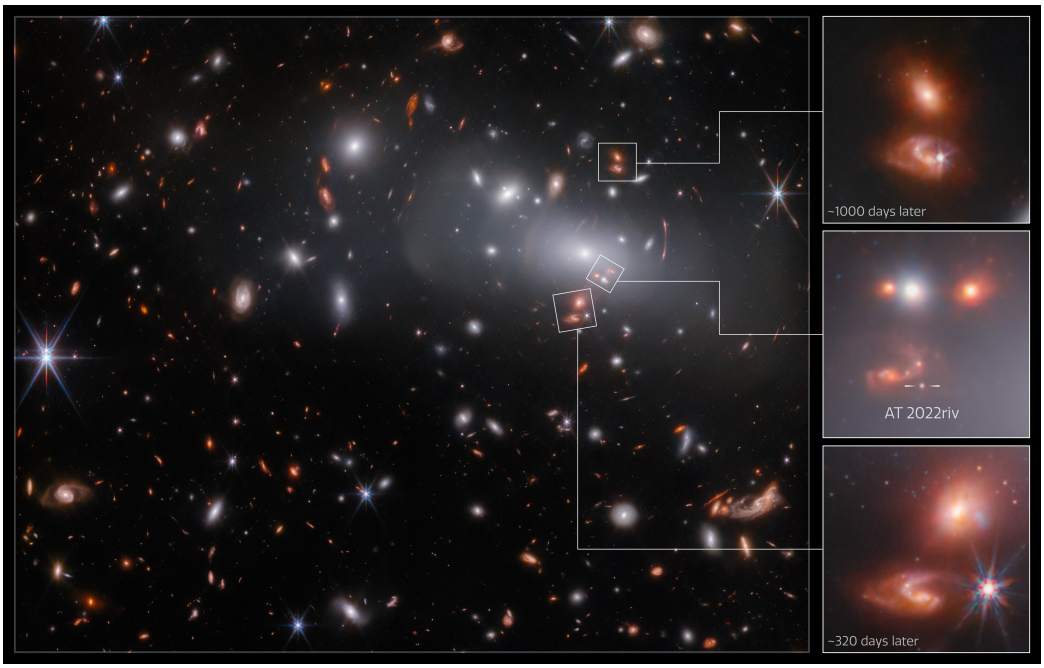

Figure 1.4: Image of RXJ 2129 containing three gravitationally-lensed images of the same supernova. Image credit: ESA/Webb, NASA & CSA, P. Kelly.

Chapter 2 is the unchanged version of a paper that has been published in *The Astrophysical Journal*. I perform photometry on three NIRCam images of RXJ 2129, identify point sources as GC candidates, and analyze their CMD and spatial distribution. I also explore subpopulations of GCs when they are divided by colour. In Chapter 3, I summarize our findings and outline future work.

In Appendix A, I discuss another strong lensing galaxy cluster, Abell 370. RXJ 2129 unfortunately does not currently have any 2-dimensional gravitational lensing maps. While we do compare the radial mass profile of RXJ 2129 to its radial GC profile, 2D maps of mass surface density of Abell 370 allow us to briefly demonstrate next steps in evaluating GCs as a dark matter probe.

Photometry is outlined concisely in Section 2.2. I describe certain steps in more detail in Appendix B, for both RXJ 2129 and Abell 370. For those looking for

more detail on performing photometry, particularly with `DAOPHOT` and IRAF, refer to Appendix B.

Chapter 2

JWST NIRCam Observations of the Globular Cluster Population of RXJ 2129.7+0005

This chapter represents an unchanged version of the paper *JWST NIRCam Observations of the Globular Cluster Population of RXJ 2129.7+0005* published in The Astrophysical Journal. The full citation follows.

Keatley, Kaitlyn and William, Harris. JWST NIRCam Observations of the Globular Cluster Population of RXJ 2129.7+0005. *The Astrophysical Journal*, 990(1):67, 2025. doi: 10.3847/1538-4357/adf5c4

Kaitlyn E. Keatley[1] and William E. Harris[1]

[1]*Department of Physics & Astronomy, McMaster University, Hamilton, ON, Canada*

Abstract

We present an analysis of the globular cluster (GC) population in the galaxy cluster RXJ 2129.7+0005 (z = 0.234) based on JWST NIRCam imaging in three filters: F115W, F150W, and F200W. We use this material to provide a detailed look at the color-magnitude distribution of the GCs and their spatial distribution around the central giant galaxy. We identified 3,160 GC candidates brighter than F150W=29.5, and assessed photometric completeness through artificial star tests. We determined that the GCs follow a radial power-law distribution with an index of 1.58 ± 0.04, with the redder GCs exhibiting a slightly greater central concentration. Their spatial distribution is also highly elliptical, closely following the shape of the brightest cluster galaxy halo light.

2.1 Introduction

Globular clusters (GCs) present numerous avenues for exploring the evolutionary histories of galaxies and galaxy clusters. GCs distribute themselves according to the gravitational potential of their host galaxies and galaxy clusters, offering insights into the history of the system. Given that galaxies in clusters reside within massive dark matter halos that dominate the gravitational field, GCs have great potential as a tool to probe these halos. Studies such as Blakeslee et al. (1997) and Harris et al. (2017) have demonstrated strong correlations between the mass of GC systems and the mass of the dark matter halo, reaffirming that regions with higher mass are expected to host more GCs.

Using simulations and kinematic models, there have been some promising results in

probing the dark matter halo using the diffuse stellar halo (e.g. Pillepich et al. (2017)) and satellite galaxies (e.g. Alabi et al. (2016), Slizewski et al. (2022)). However, these approaches face challenges: observationally measuring diffuse stellar halos is difficult at large radii, and satellite galaxy studies require highly accurate spectroscopy. In contrast, GCs are more numerous than satellite galaxies, and brighter and more extended than the diffuse stellar halo, making them highly promising tracers of dark matter in galaxy clusters.

Prior to JWST, the available resolution and sensitivity were insufficient to effectively study GC populations beyond the local universe. We have only begun to utilize the remarkable resolution and depth of JWST to study whole GC populations at intermediate redshifts. Notable examples include VV 191a (Berkheimer et al., 2024), A2744 (Harris and Reina-Campos, 2023; Harris and Reina-Campos, 2024), and SMACS J0723.3–7327 (Lee et al., 2022). These rich databases allow us to directly study ancient star clusters at earlier periods in their evolution, enabling new insights into both GC and galaxy cluster evolution.

RXJ 2129.7+0005 (hereafter referred to as RXJ 2129) is a virialized galaxy cluster at a redshift of 0.234 corresponding to a lookback time of 2.90 Gyr. It has a central BCG, a mini radio halo, a cool core (Kale et al., 2015; Giacintucci et al., 2017; Ueda et al., 2020), and an x-ray cold front in the intracluster light (ICL) demonstrating a rich merger history (Jiménez-Teja et al., 2024). Featuring several strong lensing features, RXJ 2129 was a target of the Cluster Lensing And Supernova survey with Hubble (Postman et al., 2012), leading to many strong and weak lensing studies on its mass distribution (Desprez et al. (2018); Umetsu et al. (2018); Caminha et al. (2019); Jauzac et al. (2021); Caminha et al. (2022)). The GC system has not previously been

studied.

In this paper, we utilize new high resolution JWST NIRCam images of RXJ 2129 to analyze the spatial distribution of the GCs and begin a preliminary investigation into comparisons to mass models of the galaxy cluster. This is part of a series of studies of GCs in lensing clusters that begun with A2744 (Harris and Reina-Campos, 2023; Harris and Reina-Campos, 2024). In Section 2.2, we describe our photometry procedure for detecting GC candidates and determining their magnitudes. We also perform artificial star tests to test the completeness and photometric limits of our measurements. In Sections 2.3 and 2.4, we determine the radial distribution of GCs, and investigate any trends with GC color. Additionally, we explore the angular distribution in Section 2.5, determining the significant ellipticity of the brightest cluster galaxy (BCG). In section 2.6, we compare the color-magnitude diagram and predicted metallicity to that of A2744. Finally, in Section 2.7, we summarize our findings and outline the additional work that is ongoing with RXJ 2129 and distant galaxy clusters like it.

The luminosity distance to RXJ 2129 is 1.20 Gpc, with cosmological parameters of $H_0 = 67.8$ km/s and $\Omega_\Lambda = 0.692$ (Planck Collaboration et al., 2016).

2.2 Data

We use images from JWST NIRCam in the F115W, F150W, and F200W filters drawn from the MAST JWST archive (DD 2767, PI P. Kelly). The F115W and F200W images had an exposure time of 8246 seconds, and the F150W image had an exposure time of 19927 seconds. The camera scale is $0\overset{''}{.}0307$ pixel^{-1}, with a total image size of $139\overset{''}{.}6 \times 138\overset{''}{.}9$. Figure 2.1 shows a portion of the field with the BCG.

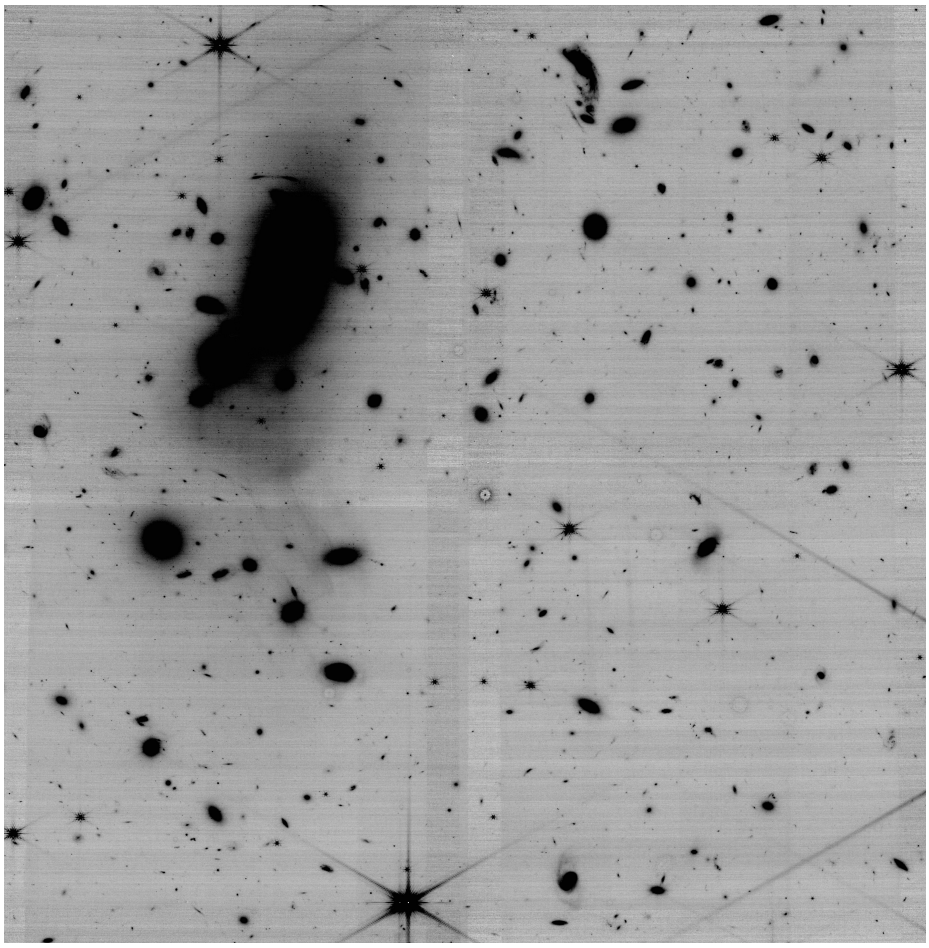

Figure 2.1: F200W view of RXJ 2129. The BCG is in the upper left. Smaller galaxies and foreground stars are also visible. Image is $139\overset{"}{.}6 \times 138\overset{"}{.}9$, which is equivalent to 534 kpc across. North is at top, and east is to the left.

2.2.1 Photometry and Object Selection

We conduct photometry and object selection using the `daophot` software (Stetson, 1987) within IRAF. First, we add the three images together to make a summed image, and then apply a median filter to eliminate large-scale gradients. With a detection threshold of $4\sigma_s$, where σ_s is the standard deviation of the sky noise, we use the *daofind* package on this median-subtracted image to find objects. The summation yields a

combined image that has relatively lower sky noise and allows for a deeper finding list of objects. For each of the three images, we use *phot* to conduct photometry using a 3px aperture radius for each object on the finding list. A point-spread function (PSF) is constructed for each filter using 46 foreground stars and a FWHM of 2.0, 2.4, and 2.8 px for the F115W, F150W, and F200W images, respectively. The interactive interface of the *PSF* package allows us to inspect the profile of each candidate star to hand-pick unsaturated, isolated foreground stars. We then run the *allstar* function to get final instrumental magnitudes on all star-like objects in our photometry list.

Allstar additionally provides *sharp* and *chi* parameters, which we use to isolate point sources by plotting these quantities against the F150W and F200W magnitudes. We make a quadratic cut in sharp-mag space, shown as orange boundaries in Figure 2.2. We reject points with a sharp value (in F150W or F200W) less than -0.75 or lying above the line $s = 0.006(m-8)^2 + 0.15$, where s is the sharp parameter and m is the uncorrected magnitude. We also remove any object that has a chi value larger than 4 in any filter. Accepted point sources are shown as black points in Figure 2.2. Additional objects near the center of the BCG were independently selected by close visual inspection and are shown as pink points.

In total, 4642 objects are recovered in all three filters using the combined finding list. Recovered point sources near the BCG are circled in red in Figure 2.3.

To convert magnitudes from the *allstar* scale to AB magnitudes, we first correct PSF *allstar* magnitudes to large aperture using bright isolated stars with a 10px aperture radius. To integrate to "infinite" radius, we use the PSF encircled energy from the NIRCam webpage[1]. Cosmological K-corrections are applied for a redshift of 0.234

[1]https://jwst-docs.stsci.edu/jwst-near-infrared-camera/nircam-performance/nircam-point-spread-functions

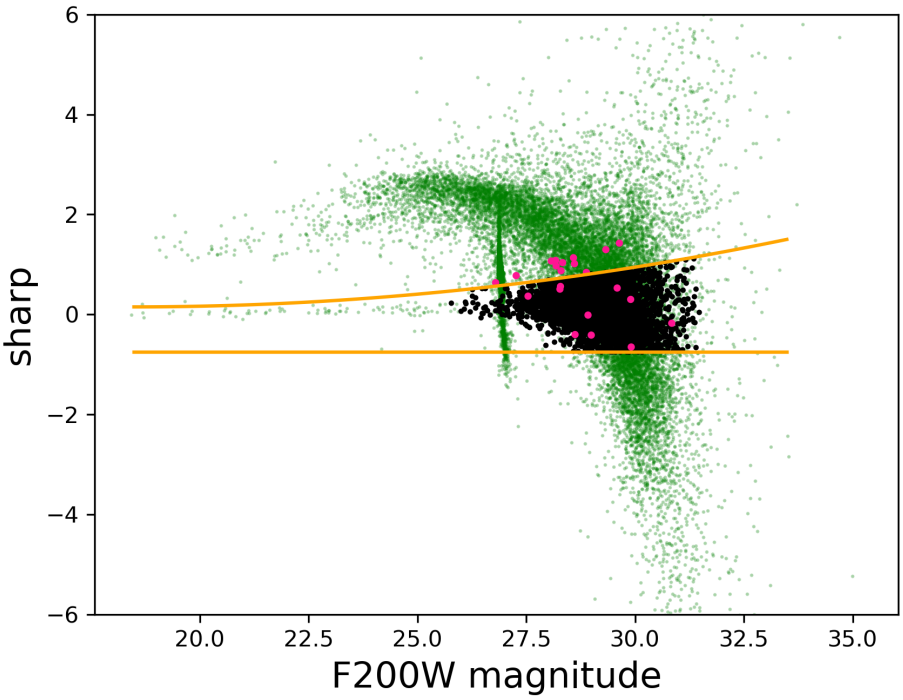

Figure 2.2: Sharp parameter of detected objects vs. magnitude in AB magnitudes. All detected objects are shown as green points. Accepted points using the sharp and chi cuts are shown in black, and selected point sources in the innermost region of the BCG are shown in pink.

using the webtool `RESCUER` (Reina-Campos and Harris, 2024). Finally, we adjust our magnitudes for foreground reddening (NASA/IPAC Extragalactic Database). Foreground absorption for RXJ 2129 is 0.040, 0.026, and 0.017; K-corrections are -0.137, -0.130, -0.370 for the F115W, F150W, and F200W filters, respectively.

2.2.2 Completeness fraction

GCs that are very faint or located in regions of high sky noise will naturally be more difficult to detect than bright, isolated GCs. To determine the completeness

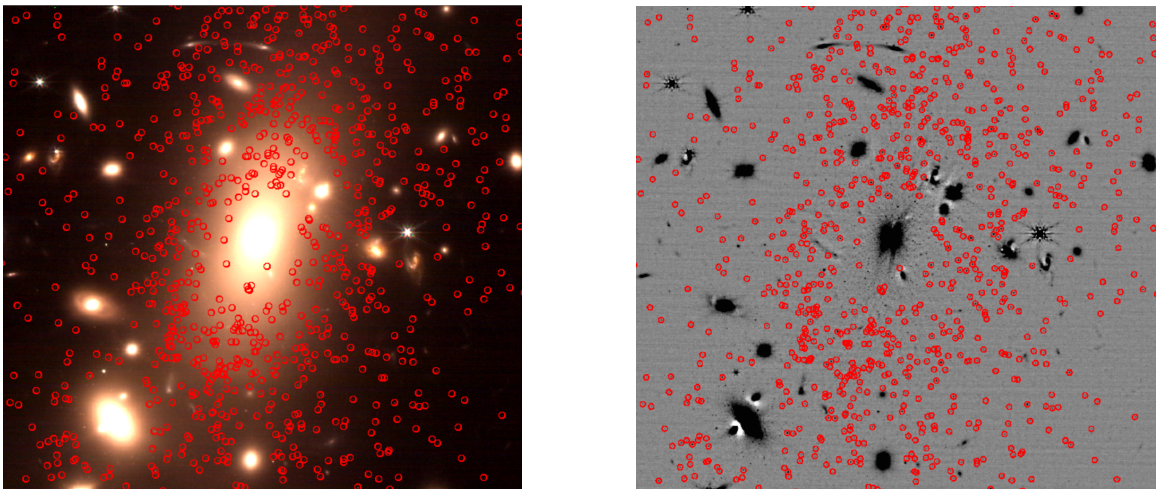

Figure 2.3: Color image (left) and unsharp-masked F200W image (right) of the field near the BCG of RXJ 2129. Point sources are circled in red. Box size is $37\overset{''}{.}3 \times 34\overset{''}{.}9$, equivalent to 143 x 133 kpc.

of our selection, we perform artificial star tests. Using the *addstar* function, we add 1060 artificial stars into each image. These stars are distributed radially to mirror the radial distribution of GCs. We use logistic regression fitting (Equation 2.2.1) to determine the recovery probability as a function of magnitude and local sky noise, as described in Harris and Speagle (2024) and Harris and Reina-Campos (2024):

$$p(m) = \frac{1}{(1 + e^{-g(x_i)})} \tag{2.2.1}$$

where $g(x_i) = \beta_0 + \beta_1 x_1 + \beta_2 x_2$. Here, x_1 is the magnitude and x_2 is the local sky noise of each object, and the β_n values are determined by the fit using the artificial stars. The local sky noise is defined as the standard deviation of the sky pixel intensities in an annulus of $0\overset{''}{.}31 - 0\overset{''}{.}46$ radii.

A maximum-likelihood solution was performed in Python using *statsmodels/scikitlearn*. Recovery probabilities of the 1060 artificial stars using the logistic regression fit are

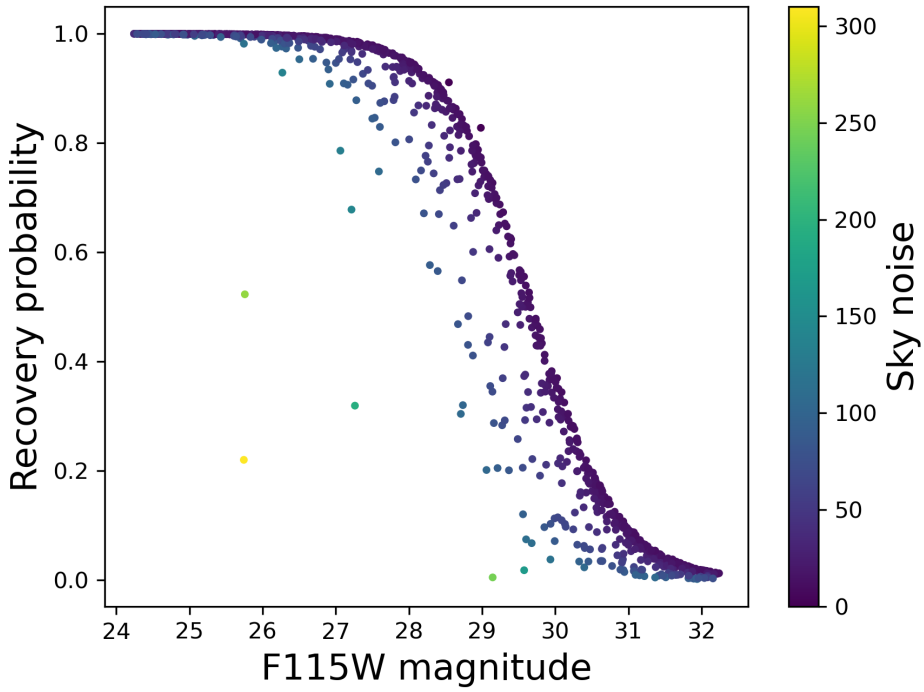

Figure 2.4: Recovery probability in the F115W filter of artificial stars using a logistic regression fit. Points are color-coded by the local sky noise. Points scattering below the main line are those in regions of higher sky background.

shown in Fig 2.4. We obtain coefficient values of $\beta_0 = 52 \pm 3$, $\beta_1 = -1.7 \pm 0.1$, and $\beta_2 = -0.027 \pm 0.004$ using corrected input magnitudes, which we use to determine the recovery probability for each of our GC candidates. We define our photometric completeness limit as the magnitude at which $p = 0.5$.

As an additional check, we also compare the input and detected magnitudes of the artificial stars to check for any systematic biases. As shown in Figure 2.5, there is a slight tendency for brighter magnitudes to be recovered for the fainter objects, but is negligible at magnitudes brighter than the completeness limit.

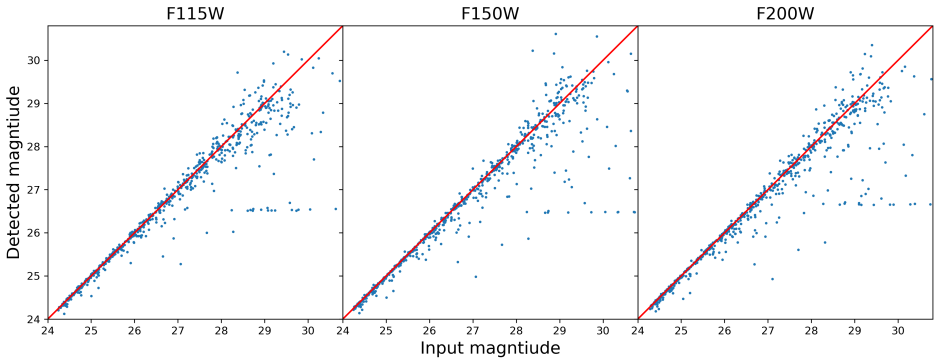

Figure 2.5: Input versus detected magnitude for 1060 artificial stars in the F115W, F150W, and F200W images. The red line shows a 1-to-1 relationship.

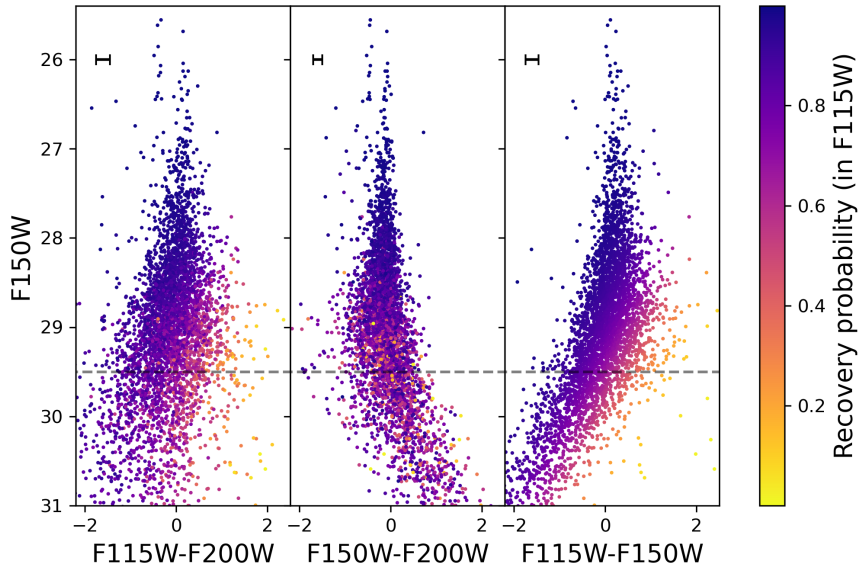

Figure 2.6: Color-magnitude diagram of point sources in RXJ 2129. Magnitudes are in AB magnitudes corrected for the cosmological K-correction and foreground reddening. Points are color-coded by the recovery probability using the logistic regression fit. The dashed line is the 50% recovery level.

We present color-magnitude diagrams of all candidate GCs in Figure 2.6, color-coded according to the recovery probability in F115W of each object. Some of the

faintest objects that passed through the culling steps may be compact background galaxies, and we also remove foreground stars as objects brighter than magnitude 25.5. The remainder of point sources are the GCs plainly clustered around the BCG. We are left with 2720 GC candidates in the magnitude range $25.5 < \text{F150W} < 29.5$. Weighted by the inverse recovery probability, and excluding objects outside of our completeness limit, our final count is 3162 GCs in our field of view of RXJ 2129. This is easily comparable to the 1000+ GCs observed in other BCGs (Harris, 2023).

2.3 Radial distribution

The spatial distribution of GCs in RXJ 2129 is of particular interest. For major galaxies, GCs typically follow a spatial distribution well described by a power-law or Sérsic profile. We plot the projected number density as a function of distance from the center of the BCG with the least squares best fitting shown in Figure 2.7. When counting GCs, we weight each object by its inverse probability of recovery to calculate a projected object count in each radial bin. Any object with a probability of recovery less than 50% in the F115W filter is removed. We exclude the innermost bin from the power-law fit as the BCG light limits our detection capabilities in this region. We find a power-law index of 1.58 ± 0.04. The background density is 0.5 arcsec^{-2}, consisting of a mix of distant GCs and faint contaminants that passed through the selection criteria.

For comparison, we also fit the distribution to a simple de Vaucouleurs profile. Shown in green in Fig 2.7, this fit also visually matches the data quite well. We find an effective radius of 157 ± 13 kpc. Chu et al. (2022) investigated surface brightness Sérsic profiles for a large collection of galaxies, including RXJ 2129. The authors found

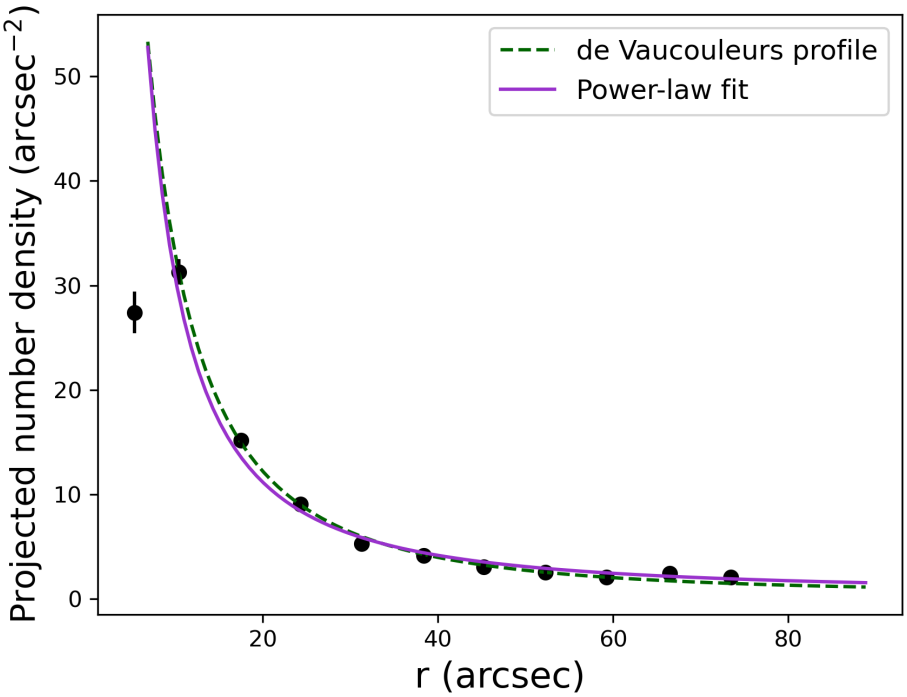

Figure 2.7: Radial distribution of the GCs fit with a power law and a de Vaucouleurs profile. Each GC count is weighted by it's inverse recovery probability, and objects with a probability of less that 50% are removed.

effective radii of 2.24, 44.48, and 190 kpc for the internal component of the BCG, the external component, and the ICL, respectively. Our GC distribution therefore has a larger effective radius than the stellar surface brightness, but a smaller effective radius than the ICL.

With a virial radius of 1.3 Mpc (Rines et al., 2013; Umetsu et al., 2018), we can be confident that we are capturing the full radial extent of RXJ 2129's GC system. Figure 2.7 shows the fit of the radial distribution out to 290 kpc – easily enclosing the 10% of the virial radius that is typically adopted for the spatial extent of GC systems (Dornan and Harris, 2023; Dornan and Harris, 2025). The effective radius of

157 kpc also lies within the expected range for BCGs (Kartha et al., 2014; Hudson and Robison, 2018).

Next, we compare our results to the total surface mass density profile modeled using strong lensing by Caminha et al. (2019). Using multiply lensed background galaxies, the authors used a pseudo-isothermal elliptical mass distribution (PIEMD; Kassiola and Kovner 1993) to model the smooth mass components. For RXJ 2129, all of the multiple images were within 100 kpc from the cluster center, which limits our comparison at larger galactocentric distances. We plot our comparison to their results in log-log space in Figure 2.8, and conclude that the GC distribution is steeper than the total mass distribution. A potential explanation for this distinction is that the dark matter profile is shallower in the center of the cluster due to its collisionless nature, while the stellar component achieves greater central concentrations. However, the present data are limited to the BCG halo region and do not explore the GC distribution across the entire field of the cluster.

2.4 Color Populations

In this section, we analyze trends and variations in relation to GC color. Through their chemical compositions, GCs record the conditions of the dark matter halos in which they formed.

GCs in large galaxies conventionally show a bimodal distribution in their color, which is closely related to their metallicity (Zinn, 1985; Barmby et al., 2000; Peng et al., 2006; Strader et al., 2007; Harris and Reina-Campos, 2023). The more metal-poor population exhibit a trend of bluer colors, older ages, and has a roughly spherical distribution. The more metal-rich GCs have redder colors, are younger, and are more

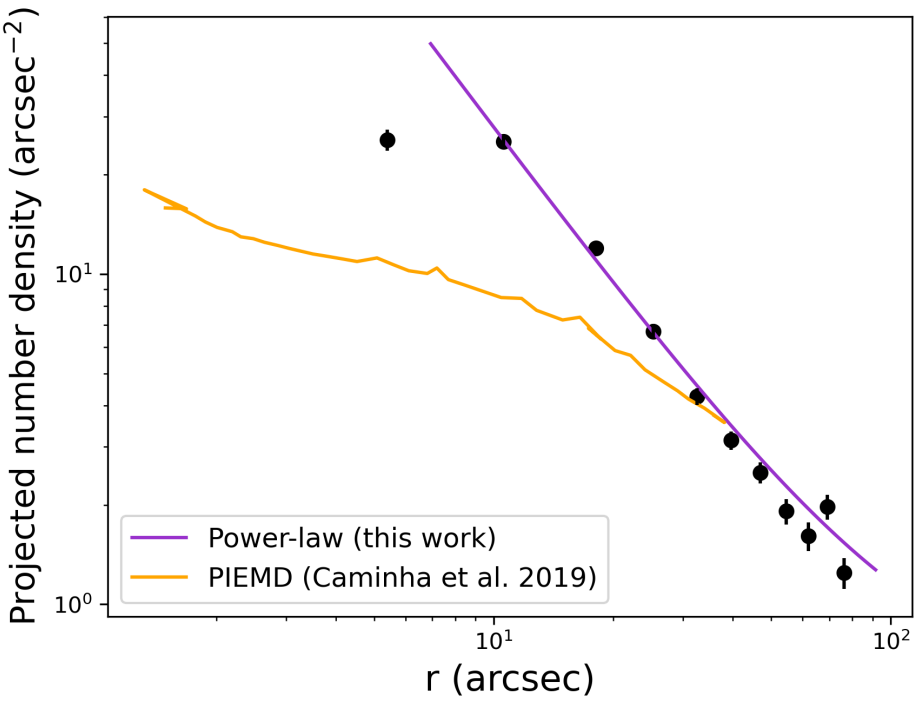

Figure 2.8: Comparison of our power-law fit for the GC radial distribution to the mass profile modeled by Caminha et al. (2019). The PIEMD profile was modeled in units of $M_\odot$ kpc^{-2} and has no meaningful normalization to the GC projected number density.

centrally concentrated. The history of the GCs is where this division originates: the more metal-rich population have been found to have mainly formed in more massive, enriched halos, while the metal-poor population formed ex situ and was later accreted (Li and Gnedin, 2019; Keller et al., 2020; Reina-Campos et al., 2022; Chen and Gnedin, 2023b).

As shown in Figure 2.6, there is no obvious division between the red and blue populations that would reflect a distinct metal-rich and metal-poor population in RXJ 2129. While it is true that some systems have shown unimodal metallicity distriubtion functions, another contributing factor is that near-infrared color indices

are less sensitive to GC metallicity than are optical colors (Harris and Reina-Campos, 2023). Additionally, there are significant measurement uncertainties in color that introduce scatter. For the present purposes, we simply divide the sample into red and blue subsets at a color of F115W−F200W= 0.018, such that each has the same projected number of GCs.

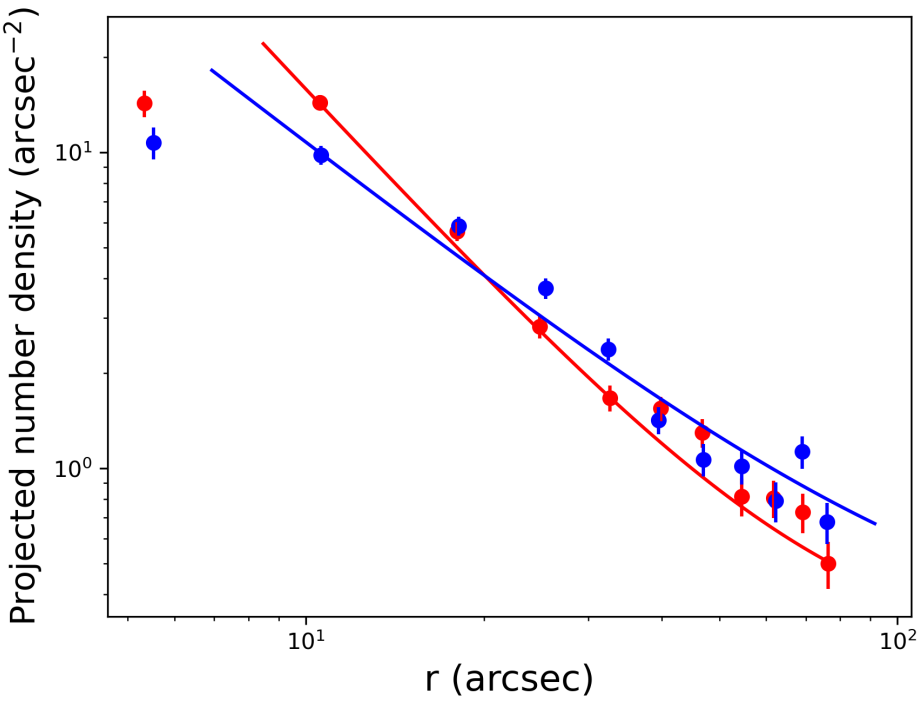

Figure 2.9: Same as Figure 2.7, but distributions are divided into red and blue subpopulations (with respective colors for data points and fit).

We repeat the radial distribution calculations and fitting on the red and blue subpopulations. The power-law indices recovered by the least squares fit are reported in Table 2.1. While a bimodality in color was not immediately visible, we do find significant distinctions when dividing the sample in half into a blue and red subsample and analyzing the spatial distribution. The redder population of GCs is more centrally

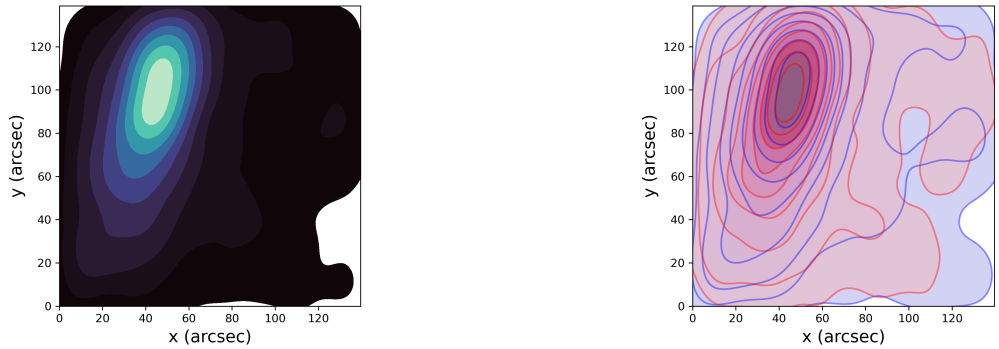

Figure 2.10: Contours of globular cluster counts. The right plot shows the contours for the red and blue populations, and the left plot shows the combined sample.

concentrated, which agrees with the expectations as a population primarily formed in situ. This is evident in the larger power-law index – reflected by the steeper slope in log space (Figure 2.9) – and the right panel of the contour map in Figure 2.10.

2.5 Ellipticity

As we can see in Fig 2.10, the distribution of GCs is highly elliptical, as is the BCG light profile itself. Our analysis in the previous section assumes circular bins, but we would now like to account for elliptical annuli. We can determine the ellipticity and position angle of the BCG using the expression for GC distribution given by McLaughlin et al. (1994):

$$\sigma(R,\theta) = kR^{-\alpha}[\cos^2(\theta-\theta_p) + (1-\epsilon)^2\sin^2(\theta-\theta_p)]^{-\alpha/2}$$
$$\equiv kR^{-\alpha}f(\theta) \quad (2.5.1)$$

where θ_p is the position angle of the semi-major axis, ϵ is the ellipticity, k is a normalization constant, and α is the power-law index obtained from the number density fit. To isolate the angular component, we plot $f(\theta)$ as a function of position angle θ:

$$f(\theta) = [\cos^2(\theta - \theta_p) + (1-\epsilon)^2 \sin^2(\theta - \theta_p)]^{-\alpha/2} \tag{2.5.2}$$

GCs are counted and normalized within azimuthal bins using an inner radius of 3".69 and an outer radius of 24".60. These values are chosen such that there is no significant influence from the incompleteness at the center of the BCG, and we are capturing the elliptical behavior without looking too far out into the intergalactic medium.

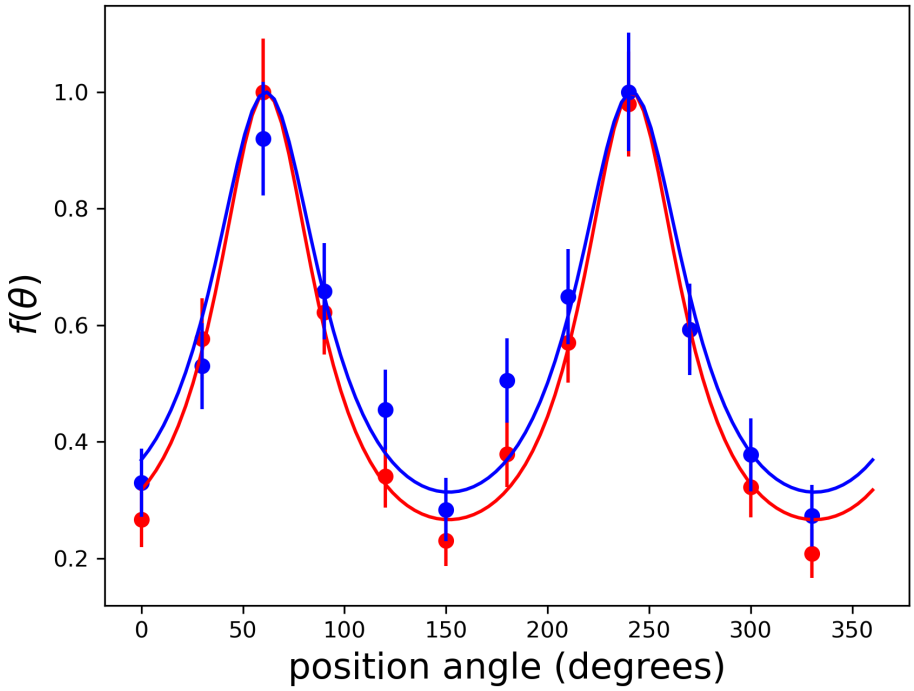

Figure 2.11: Normalized azimuthal number density profile for red and blue GC samples.

We find an ellipticity of 0.54 ± 0.01 and a position angle of the semi-major axis of $61° \pm 2°$ degrees north of west (counterclockwise from the positive x-axis) for the full sample. This agrees quite well with the ellipticity of 0.67 and position angle of 66°.3 for the stellar light determined by Caminha et al. (2019). Once again, we repeat the process for the red and blue subpopulations; these values are reported in Table 2.1, and $f(\theta)$ is plotted in Figure 2.11.

Sample	Power-law Index	Ellipticity	Position Angle (deg)
All sources	1.58 ± 0.04	0.54 ± 0.01	61 ± 2
Red sources	1.92 ± 0.04	0.56 ± 0.01	61 ± 1
Blue sources	1.42 ± 0.1	0.51 ± 0.02	61 ± 2

Table 2.1: Parameters from the radial and angular best fits for the full sample of point sources, the red subsample, and the blue subsample.

As expected, the red population has a greater ellipticity, reminiscent of the interpretation that that these GCs are primarily formed within the galaxy cluster and will more closely match the shape of the galaxies. The bluer population of GCs is less elliptical, which is consistent with the view that it has a higher proportion of accreted objects. The position angle of the semimajor axis is consistent between the two populations.

2.6 Comparison to A2744

A2744, another massive strong lensing galaxy cluster whose GCs have been intensively studied, has a redshift of 0.308, corresponding to a lookback time of 3.5 Gyr. In Figure 2.12, we compare the absolute magnitude of the RXJ 2129 GC candidates to those in A2744, determined by Harris and Reina-Campos (2023). The A2744 population

reaches higher-luminosity GCs, likely as a consequence of being a more populous system and having a younger stellar population by ~ 0.6 Gyr. On the other hand, dimmer luminosities are achieved in RXJ 2129. The mean colors for the three indices are displayed in Table 2.2; good agreement is seen between the two sets of data. The rms scatters around 0 in the three color indices average 118 for RXJ 2129 and 191 for A2744.

System	(F115W-F200W)	(F150W-F200W)	(F115W-F150W)	N
RXJ 2129	0.05 ± 0.01	-0.20 ± 0.01	0.25 ± 0.01	797
A2744	-0.027 ± 0.003	-0.219 ± 0.004	0.193 ± 0.004	5281

Table 2.2: Mean K-corrected color and error on the mean for RXJ 2129 and A2744 (Harris and Reina-Campos, 2023) objects brighter than $F150W_0$=-12.

RXJ 2129 has 797 objects brighter than $F150W_0 = -12$, only a fraction of the population observed in A2744. To enable a fair comparison, we randomly select a subsample of 797 objects from A2744. The color-magnitude diagrams and luminosity functions for both RXJ 2129 and this matched A2744 sample are shown in Figure 2.13. We note that our observations sample only the brightest end of the GC luminosity function (GCLF), well above the turnover point. The GCLF turnover is nearly universal at $10^5 L_\odot$ (corresponding to $M_{150} = -8.3$), with only a weak dependence on host galaxy mass (Harris et al., 2014). With a completeness limit of F150W=29.5, or $M_{150} = -10.8$, our luminosity limit is around $10^6 L_\odot$, meaning we are only detecting the most luminous GCs.

In Figures 2.14 and 2.15, we show predicted color-metallicity and luminosity-age relations for GC populations of different ages and metallicities. These are generated using the PARSECv1.2S CMD3.7 single-burst stellar population models[2] (Bressan

[2] `https://stev.oapd.inaf.it/cgi-bin/cmd_3.7`

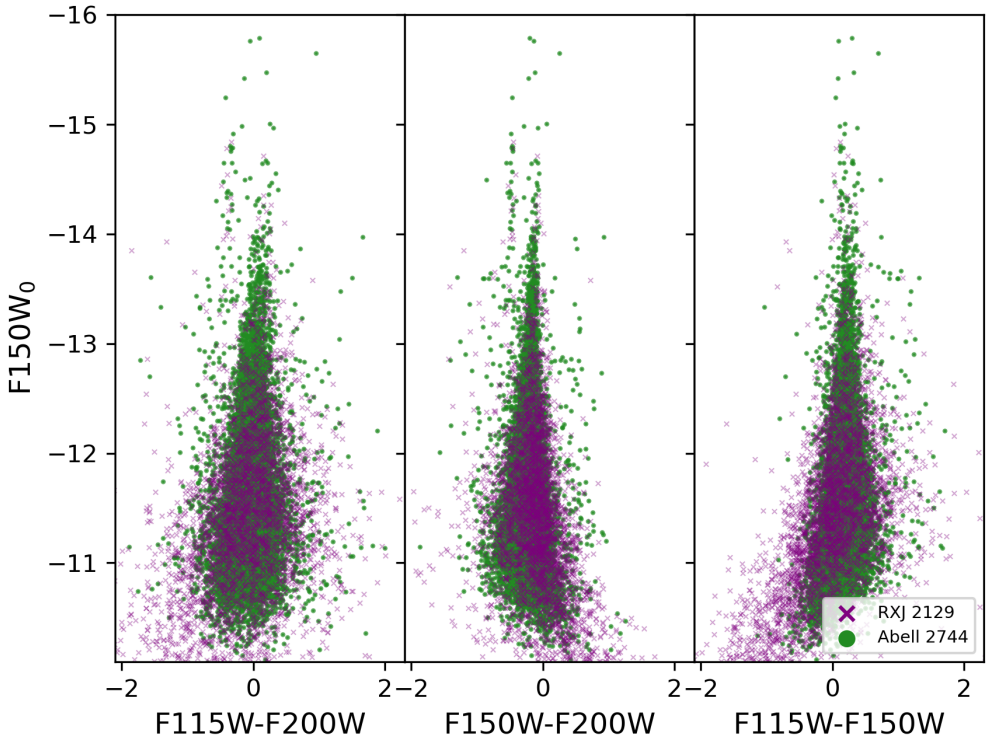

Figure 2.12: Color-magnitude diagram of point sources in RXJ 2129 and Abell 2744 (Harris and Reina-Campos, 2023).

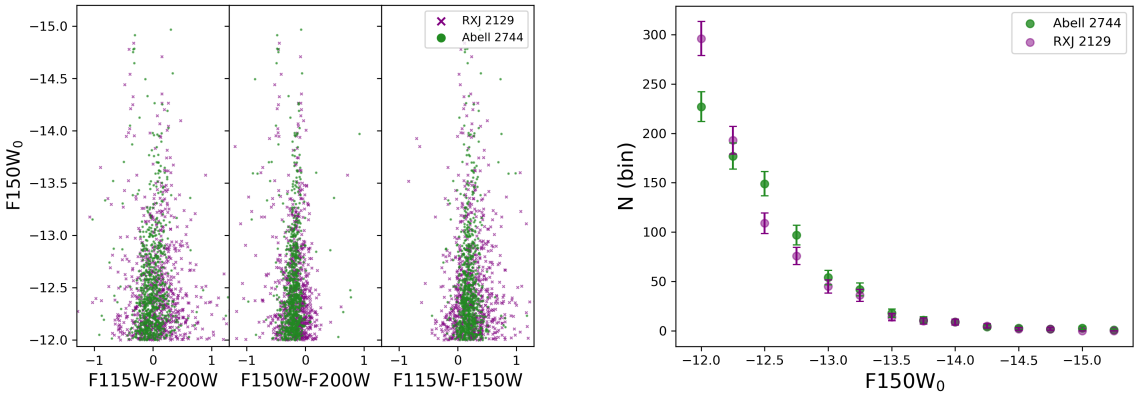

Figure 2.13: Color-magnitude diagram of point sources in RXJ 2129 and A2744 for 797 objects (left) and number of objects observed in 0.25 mag bins in F150W$_0$ (right).

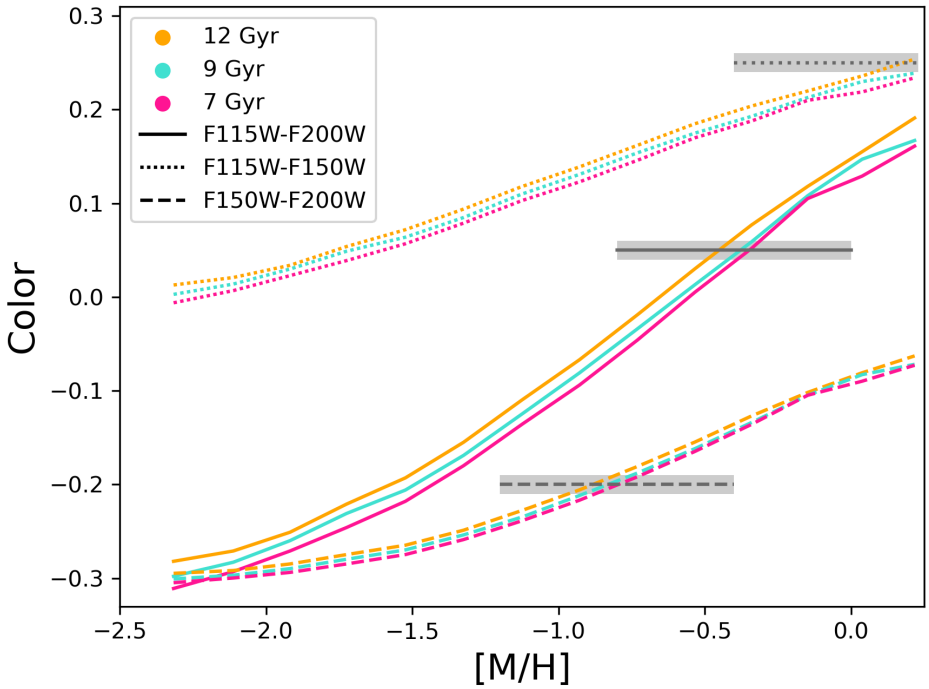

Figure 2.14: Predicted color-metallicity relations from the PARSEC CMD3.7 single-burst stellar population models. Colors and linestyles indicate the assumed ages and color indices (AB magnitudes). Grey lines indicate the mean color of RXJ 2129 GCs, as reported in Table 2.2, with shaded regions indicating the errors on the mean.

et al., 2012). We can see that color (plotted in AB magnitudes) is fairly insensitive to age in these filters. Gray lines in Figure 2.14 mark the intersection between the observed colors and the predicted color-metallicity functions; the mean metallicity of the RXJ 2129 GCs above $F150W_0 = -12$ is estimated to be [M/H]~ -0.4. We put the most reliance on the F115W-F200W filter, as it has the strongest relationship with metallicity. This value agrees with A2744 within the combined uncertainties of the photometry and the K-corrections.

Figure 2.15 shows that the relative evolution in luminosity with age is only weakly

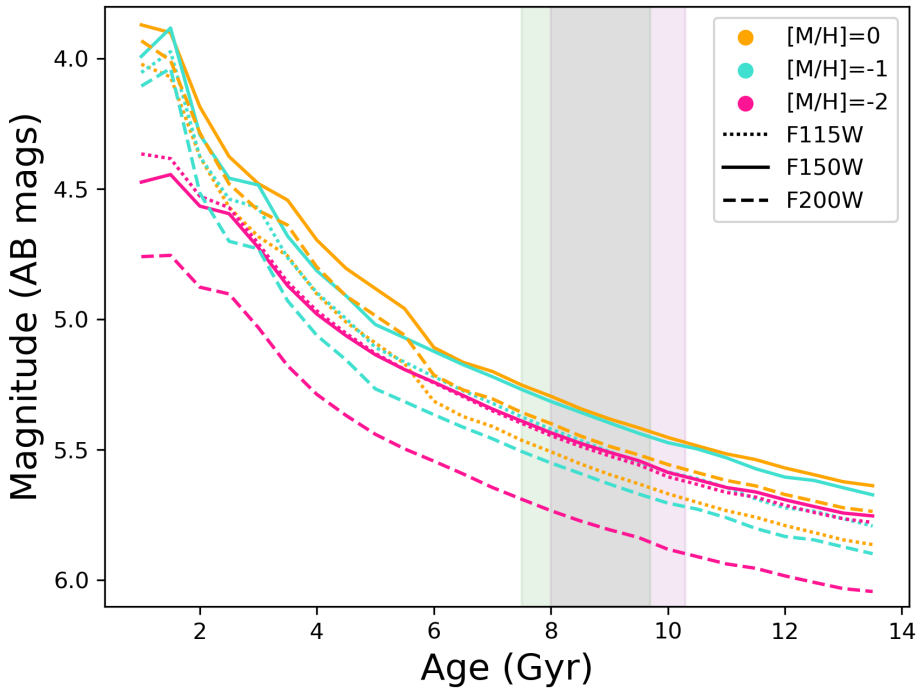

Figure 2.15: Predicted luminosity-age relations from the PARSEC CMD3.7 models. Colors and linestyles indicate the assumed metallicity and NIRCam filter. Shaded regions show the expected age range of GCs in RXJ 2129 (purple) and Abell 2744 (green).

dependent on metallicity or filter choice, indicating that these bands are well-suited for comparing GC populations across different redshifts. Assuming an age range of 2-3 Gyr (as observed in Milky Way GCs, e.g. Leaman et al. (2013)), beginning ∼0.5 Gyr after the formation of the galaxy cluster, we highlight this interval as shaded regions in Fig 2.15 to represent the plausible age range of the GC populations.

The GCs of Abell 2744 and RXJ 2129 have very similar CMDs, luminosity functions, and metallicity within our completeness limit. The similarity despite their difference in lookback time is consistent with the idea that these populations formed at similarly early epochs, and have undergone little subsequent evolution besides a

gradual decrease in luminosity over the additional 0.6 Gyr. A comparison over a larger range of ages would be possible if local GC systems were imaged in the JWST near-infrared wavelengths.

2.7 Summary and Conclusions

In this study, we have resolved and analyzed the population of GCs in the galaxy cluster RXJ 2129 at a redshift of 0.234. We conducted photometry on three images of RXJ 2129 from JWST NIRCam and found 2720 GC candidates that appeared in the F115W, F150W, and F200W filters. We explored the completeness and photometric limits of our measurements by inserting artificial stars and fitting with a logistic regression function. Weighted by the inverse recovery probability of each object, our projected count is 3160 ± 60 GCs brighter than F150W = 29.5.

We have analyzed the radial and angular distribution of GCs from the center of the BCG, and compared to radial models of the surface brightness and total mass distribution predicted by previous studies on RXJ 2129. The distribution of the GCs around the BCG follows a radial power law with an index of 1.58 ± 0.04. We also determined the ellipticity of the GC distributions and position angle of the semimajor axis to reflect the shape of the BCG. When divided into a red and blue population, the redder GCs have a steeper power-law fit and a greater ellipticity. They are more centrally concentrated than their bluer counterparts, agreeing with predictions that redder GCs are primarily formed in situ while bluer GCs are primarily accreted.

Our future goals are to compare the spatial distributions of the GCs in two dimensions to the total mass distribution. Using gravitational lensing maps, we can probe the gravitational field of the cluster, leading to further evaluation of the strength of

GCs as a tracer for dark matter in galaxy clusters.

RXJ 2129 can be added to the growing series of giant galaxies in lensing clusters whose GCs can now be studied with deep JWST imaging. It will soon be possible to study such systems over lookback times extending up to 6 Gyr and beyond, and build up an observationally based picture of GC system evolution.

Acknowledgments

We acknowledge financial support from the Natural Sciences and Engineering Research Council of Canada (NSERC). K.K. acknowledges support by the Ontario Student Assistance Program with an Ontario Graduate Scholarship. We would also like to thank Marta Reina-Campos for the helpful discussion and ongoing collaboration.

Data Availability

The JWST images of RXJ 2129 are publicly available at doi: 10.17909/q8pr-dt43.

Facility: JWST(NIRCam)

Software: Daophot (Stetson, 1987), ds9 (Joye and Mandel, 2003), IRAF (Tody, 1986, 1993), Matplotlib (Hunter, 2007), NumPy (Harris et al., 2020), PARSECv1.2S (Bressan et al., 2012), pyraf (Science Software Branch at STScI, 2012), seaborn (Waskom, 2021), statsmodels (Seabold and Perktold, 2010)

Chapter 3

Conclusion

3.1 Summary and Conclusions

Relics of high-pressure star formation in the early universe, GCs at all redshifts are treasure troves of information. In the local universe, resolved photometric and spectroscopic studies have explored unique chemical signatures, kinematics, and subpopulations. Our understanding of GC formation and evolution, however, remains largely theoretical, since the conditions required to form YMCs are disfavoured at later times. With JWST's remarkable resolving power, GC studies are entering a new era: observations can now be extended to intermediate redshift. Further understanding of these star clusters and their undiscovered potential requires the slow and steady accumulation of data on intermediate redshift systems.

In Chapter 2, I presented an in-depth photometric analysis of the galaxy cluster RXJ 2129 at redshift 0.234. Using the `daophot` software within IRAF, I built a PSF for each filter, isolated point sources, and assessed the photometric limits and completeness using artificial star tests. I identified 2720 candidate GCs brighter than

F150W= 29.5. After excluding uncertain detections and weighting the remaining objects by the inverse of their recovery probability, my projected count is 3160 ± 60.

I constructed CMDs and compared to Abell 2744, finding good agreement in both mean colour and luminosity range. I thoroughly investigated the spatial distribution of GCs around the BCG of RXJ 2129 in both radial and azimuthal dimensions. The population follows a radial power-law profile with a power-law index of $\alpha = 1.58 \pm 0.04$; this is steeper than the total mass profile inferred from strong lensing. The distribution of GCs – like the BCG – show considerable ellipticity. I find an ellipticity of 0.54 ± 0.01: comparable but slightly smaller than previous estimates for the BCG.

The relation between NIRCam colour indices and metallicity is shallow, making it difficult to confidently determine average metallicity or to separate subpopulations. Nonetheless, armed with our knowledge on red and blue subpopulations of GCs in the nearby universe, I divide the sample into red and blue halves and re-examine their spatial distributions. I find significant difference between the two subsamples; the power-law indices differ at the 5σ level and ellipticities at 3σ. Position angles are consistent, as expected from a well-mixed, virialized system. Overall, the redder GCs are more centrally concentrated and have a more elliptical distribution around the BCG, while the bluer GCs have a wider and more circular distribution. This is consistent with the behaviour of metal-rich and metal-poor GCs described in Section 1.2.

3.2 Future Work

As JWST images pour in, more and more galaxy clusters await photometric analysis of their GC populations. Building comparable datasets for lensing clusters over a range of redshifts will allow us to trace the systematic evolution of the GC population in the CMD. A challenge arises: JWST near-infrared filters are used for GC populations $z \gtrsim 0.05$, while HST optical filters are used in the nearby universe. It is possible to compare CMDs of different colour indices using transformations from stellar models (e.g. PARSEC), though it introduces errors. Ideally, we would have consistent filter coverage is available across epochs. As a start, we need to image a nearby galaxy cluster with a rich GC population with JWST.

Multi-wavelength photometry will enable spectral energy distribution (SED) fitting and new derivations of GC metallicity and age. This has been demonstrated for GC populations by Faisst et al. (2022), Hartman et al. (2025), and Kim et al. (in prep). For RXJ 2129, Jiménez-Teja et al. (2024) performed SED fitting on the ICL light using JWST+HST images; additional JWST bands would allow the same analysis to be applied to its GCs. Compared to colour indices alone (as in this work), SED fitting yields far more reliable metallicity estimates.

Finally, the next exciting frontier is the use of GCs to probe dark matter and galaxy assembly. Spatial distribution of GCs across the field can be compared with the gravitational potential as derived from lensing maps. This will also need to be performed for a range of target fields and redshifts. Upcoming work by Reina-Campos et al. (in prep) will compare GC distribution with the total projected mass of galaxy clusters through a probabilistic analysis, laying important groundwork. For a qualitative sneak peek, see Fig. A.2, where GC spatial density contours are plotted

on top of total mass surface density for Abell 370. As the capabilities of our telescopes grow, so too does the wealth of usages for GC systems in understanding the evolution of galaxy clusters and the broader universe.

Appendix A

Abell 370

This Appendix chapter considers Abell 370 – another massive strong lensing galaxy cluster. While RXJ 2129 does not currently have 2-dimensional lensing maps, Abell 370 *does*. I take this opportunity to demonstrate a proof of concept – that the GC distribution does indeed correlate well with the dark matter halo. Future work will expand this quantitatively as outlined in Section 3.2.

Abell 370 has two BCGs, making it a more complex system than RXJ 2129. At redshift 0.375, Abell 370 has a lookback time of 4.1 Gyr. Its luminosity distance is 2.07 Gpc. Abell 370 sports a collection of strong and weak lensing studies on its mass distribution, including Richard et al. (2010); Lagattuta et al. (2017); Diego et al. (2018); Strait et al. (2018); Gledhill et al. (2024).

We use NIRCam images in the filters F090W, F115W, F150W, and F200W. The image scale is 0.02 "/px. The photometric procedure for processing the images and isolating point sources is the same as for RXJ 2129, outline in Section 2.2. Appendix B provides more detail. The CMD of point sources in Abell 370 is shown in Fig. A.1. A similar analysis as we've described for RXJ 2129 could be performed for completeness

testing, spatial and azimuthal distribution of Abell 370's GCs, and subpopulations.

In Fig. A.2, we overlay GC spatial density contours on the convergence (κ) map produced by Strait et al. (2018). For a source at $z = 9$, κ is the projected surface mass density scaled by a critical surface density, which depends on the relative distances between the observer, lens, and source. Strong lensing is possible where $\kappa \geq 1$. The peaks in both GC spatial density and dark matter projected surface density align well with the two BCGs, and align very well with each other! Future work will quantitatively evaluate this by generating a hypothetical GC population from the lensing map and comparing it to the observed population.

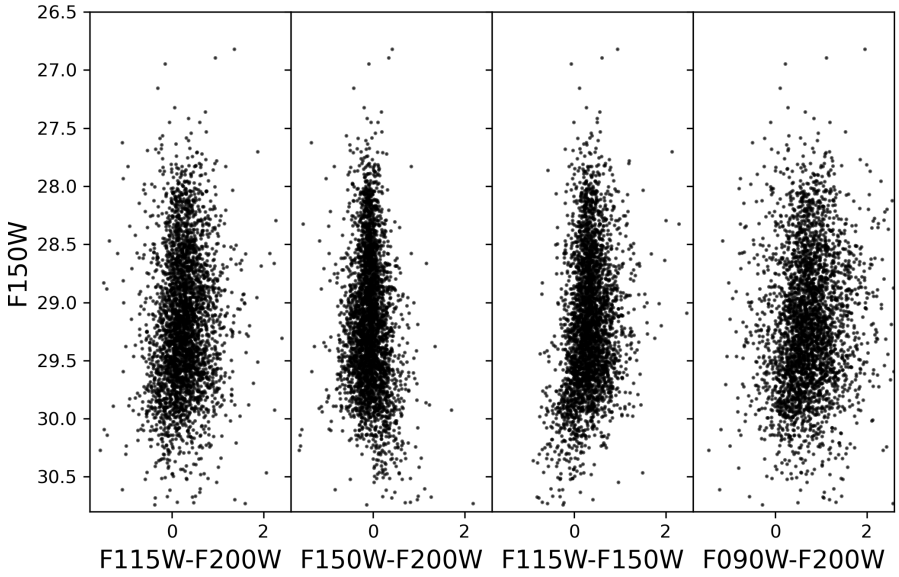

Figure A.1: Colour-magnitude diagram of point sources within 2000px of either of Abell 370's BCGs. Magnitudes are AB magnitudes, corrected for cosmological K correction and foreground reddening.

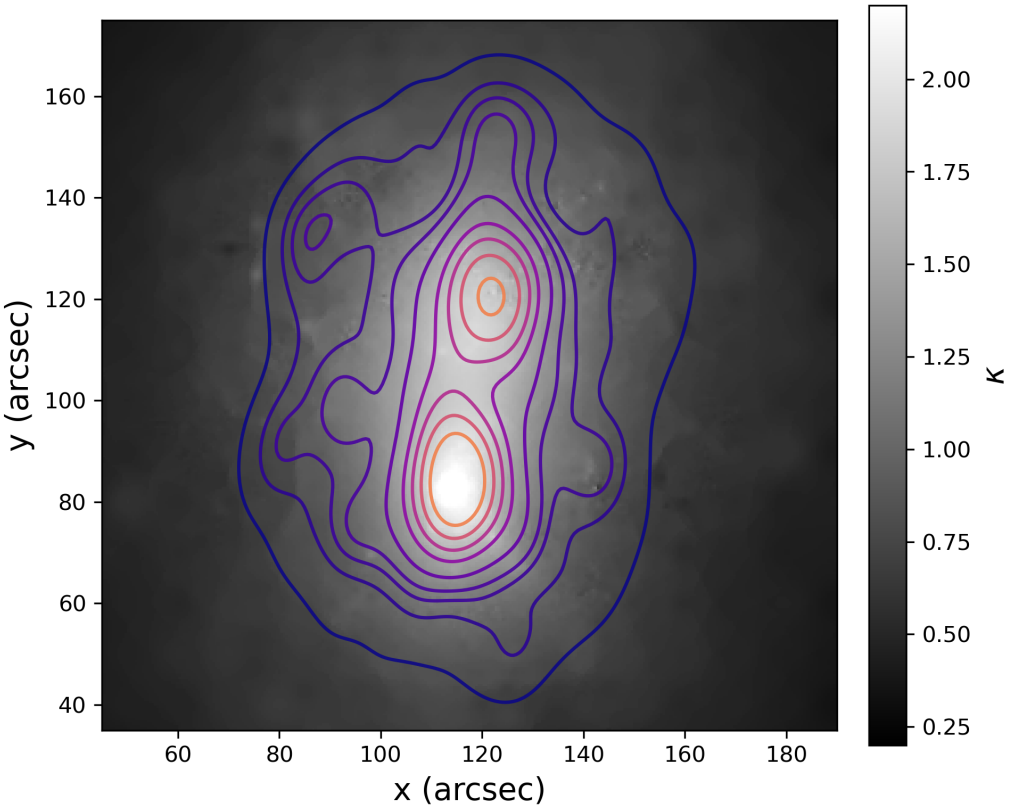

Figure A.2: Convergence (κ) map of Abell 370 lensing models produced by Strait et al. (2018). Contours are GC spatial density, representing a total of 3300 candidates.

Appendix B

Photometry with IRAF

In this section, I discuss the photometry process in more detail, including building the PSF, isolating point sources, and correcting magnitudes with DAOPHOT.

B.1 PSF

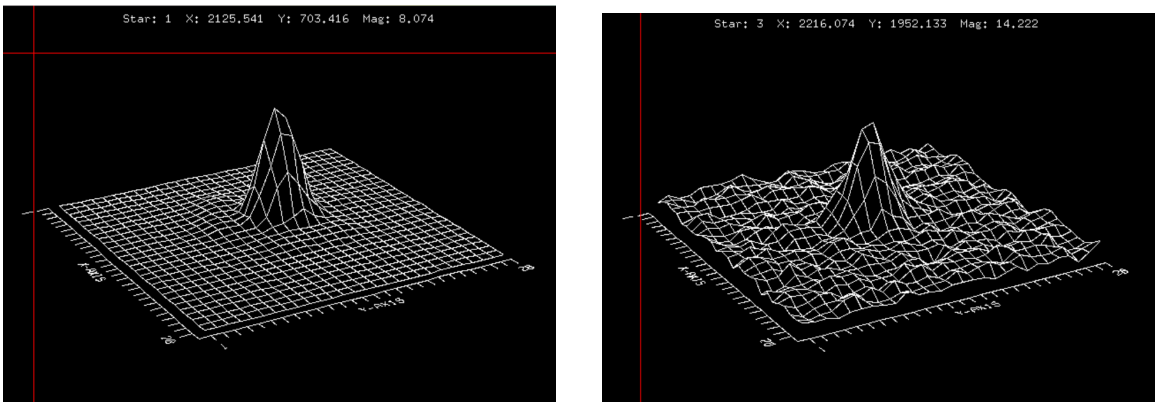

Figure B.1: Profiles of a bright foreground star (left) and a dim foreground star (right) in the interactive window of the *psf* program within DAOPHOT.

Building the PSF is a crucial step in doing successful photometry. The *pstsel*

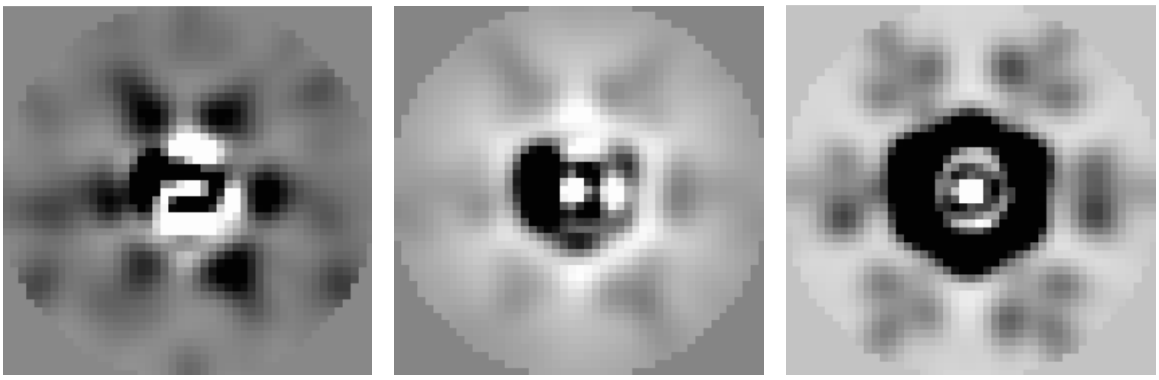

Figure B.2: PSFs constructed using foreground stars in the field of **RXJ 2129**. PSFs from left to right are for the F115W, F150W, and F200W filters, respectively.

function in `DAOPHOT` takes in the finding list of objects and returns the ones that are the most stellar-like (alternatively an existing list of star coordinates can be input). The *psf* function then compiles the PSF using the profile of accepted stars. The *psf* program runs through five possible models and chooses the best fit: *gaussian, lorentz, moffat15, moffat25, penny1*, or *penny2*. The interactive window allows the user to inspect the profile of each star before accepting it. PSF stars should be isolated and unsaturated. Examples of two accepted stars are shown in Fig. B.1. Compiled PSFs for RXJ 2192 in each filter are shown in Fig. B.2; diffraction spikes are visible in all three.

B.2 Isolating point sources

In section 2.2, I refer to *chi* and *merr* parameters that are returned along with *sharp* of selected objects from *allstar*. While *sharp* is the primary parameter used in selecting point sources, the others are useful in the initial steps.

Fig. B.3 and Fig. B.5 show *merr, sharp,* and *chi* parameters plotted against

magnitude for RXJ 2129 and Abell 370. The left panels are all objects that are returned by *allstar*; the right panels highlight accepted point sources in black and pink. The accepted lists went through many iterations and required some trial and error. RXJ 2129 posed an additional challenge, because the bright and noisy BCG light interfered with detections in the innermost region. Visual inspection, while tedious, is sometimes useful. Points within the ellipse shown in Fig. B.4 were visually identified as GC candidates and allowed some leniency in their *sharp* value. This was not necessary for Abell 370 thanks to the greater depth of the images. Quadratic limits on positive and negative sharp values often work well as there is a greater degree of scatter for fainter objects. I ultimately choose to use a quadratic cut on positive values of *sharp* and a linear cut as the lower limit. *chi* (χ^2 of the PSF fit for each object) was given an upper limit in all filters.

B.3 Magnitude correction

.als magnitudes are converted into instrumental magnitudes using Equation B.3. Aperture photometry was originally performed with a small aperture: aperture radius of 3px, sky annulus with inner radius of 10px and width of 5px. This captures the centre of the stellar profile while missing the wings. We use a larger aperture to capture the wings of the PSF out to 10px, then extrapolate to infinity. A radius aperture is performed with a sky annulus inner radius of 60px and width of 10px. This correction term, Δm, is determined by plotting the difference in magnitude between the small and large aperture photometry against the 3px aperture magnitude (Fig. B.6, Fig. B.7).

Next, the PSF wings are extrapolated using the encircled energy curves provided

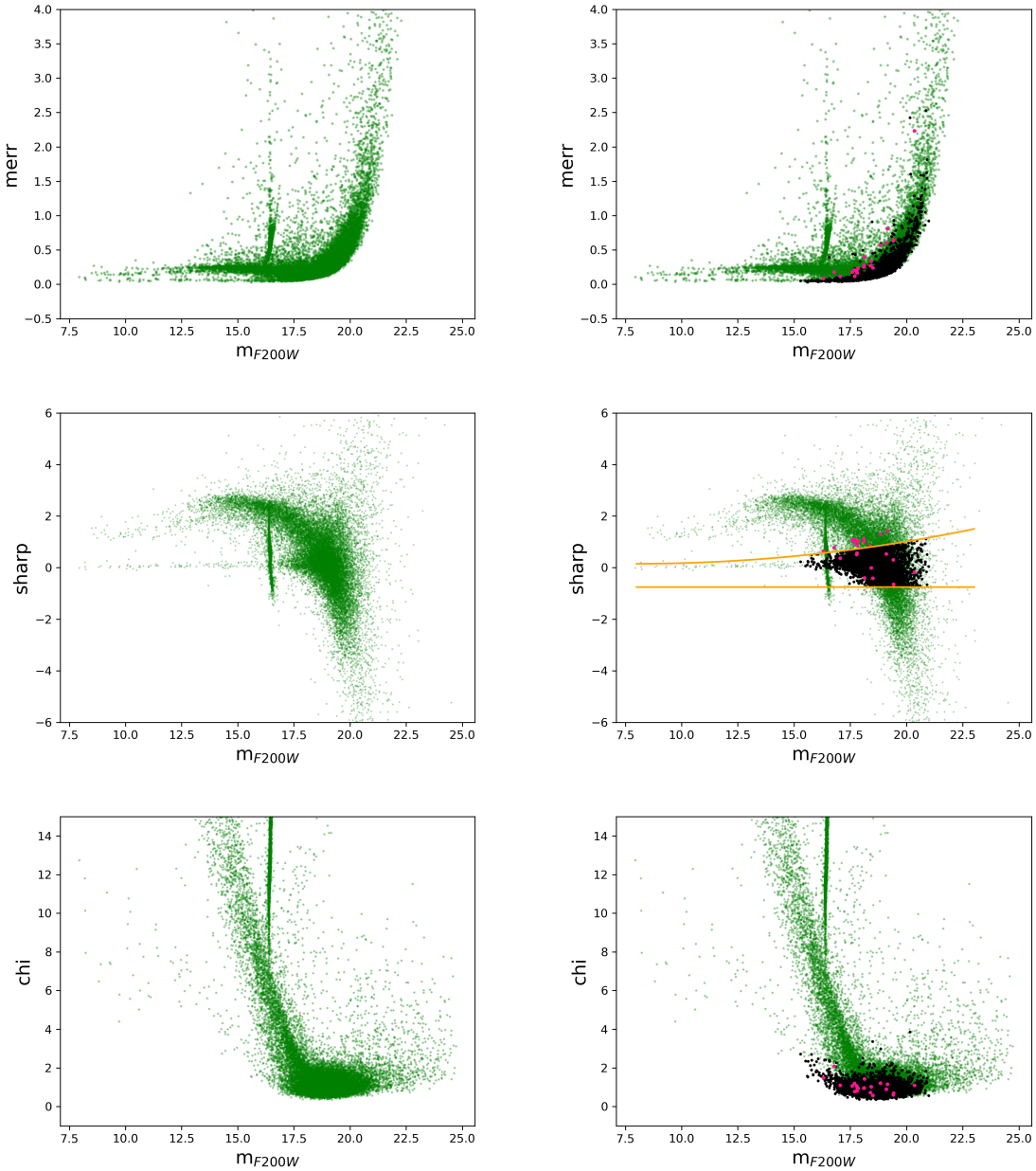

Figure B.3: *merr, sharp,* and *chi* of **RXJ 2129** candidate objects. The left column shows all objects return by *allstar* (39,650 objects); the right column shows accepted point sources in black and pink points (3969 objects).

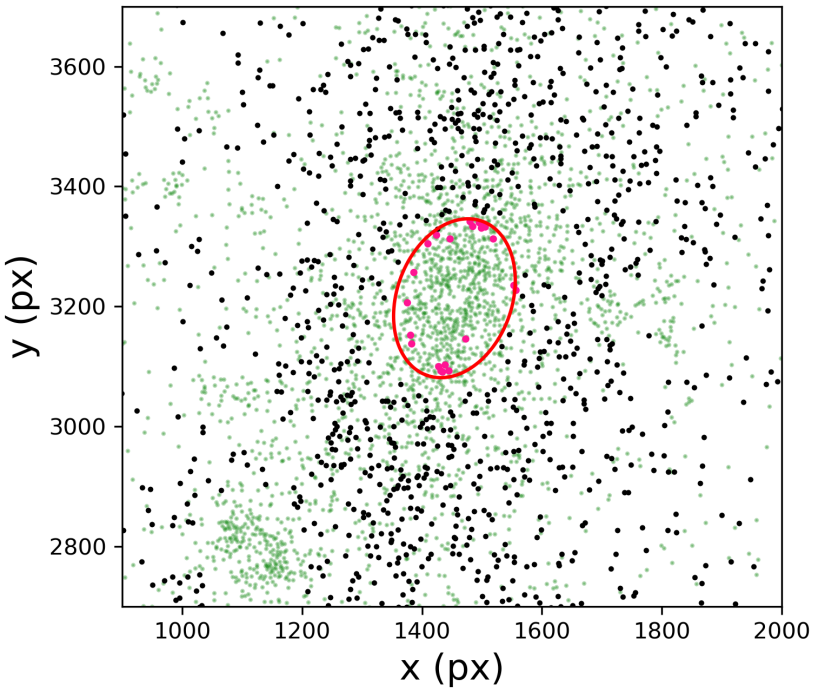

Figure B.4: Coordinates of all objects (green) and point sources (black) clustered around the BCG. The pink circle shows the area in which independent criteria was used to identify point sources.

in the JWST documentation (see Section 2.2 for link). The encircled energy fraction (EEF) at an aperture radius of 10px is taken for each filter, and contributes the following correction factor:

$$m_{EE} = 2.5 \log EEF \tag{B.3.1}$$

The correction factor to convert from `DAOPHOT` *allstar* output magnitudes to AB magnitudes is given by:

$$m_{corr,\lambda} = 2.5 \log (1000\,\mathrm{s}) - \Delta m + m_{EE} + ZP_{AB} - ZP_{daophot} - k_\lambda - A_\lambda \tag{B.3.2}$$

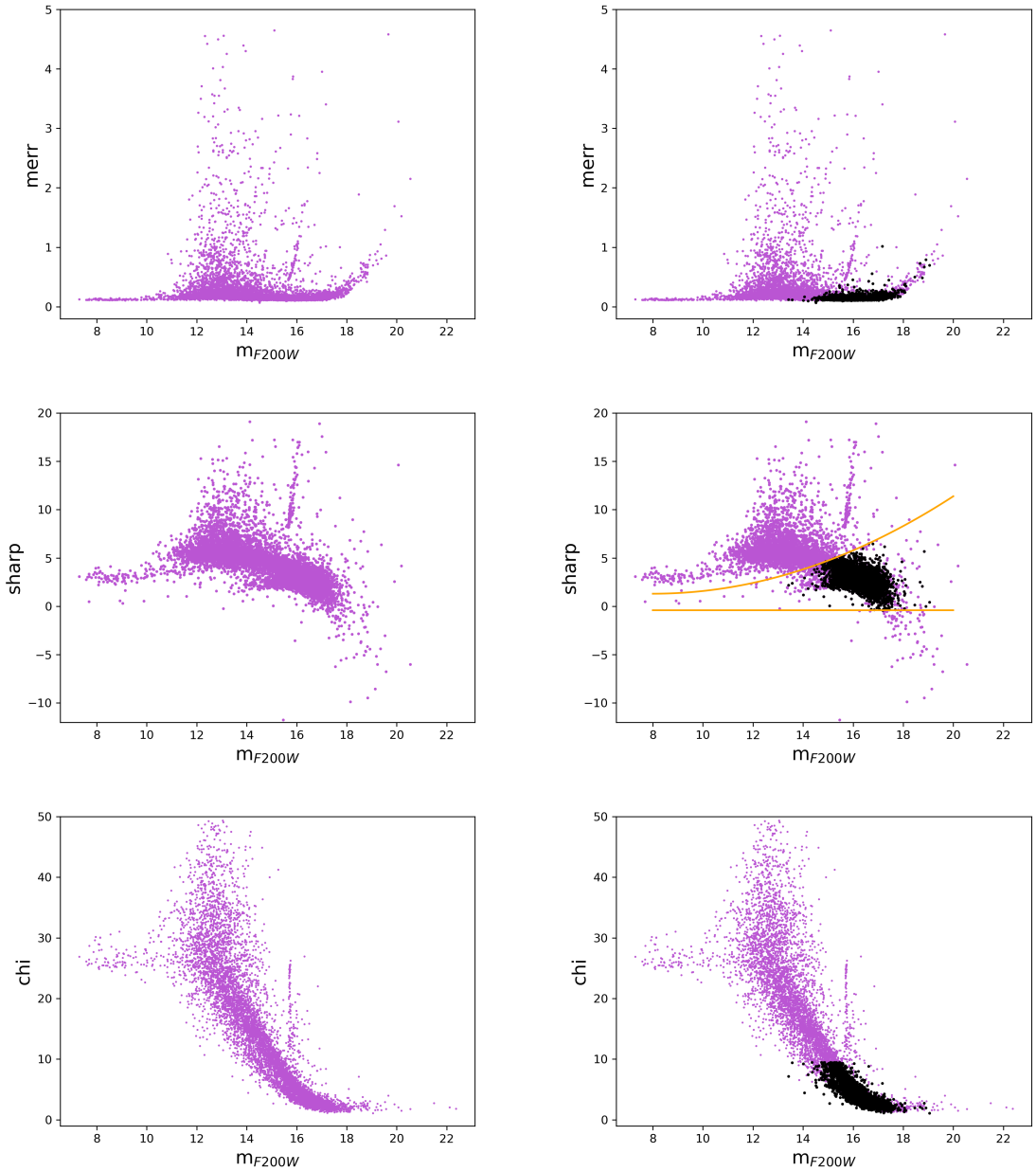

Figure B.5: *merr, sharp,* and *chi* of **Abell 370** candidate objects. The left column shows all objects return by *allstar* (8029 objects); the right column shows accepted point sources in black points (3299 objects).

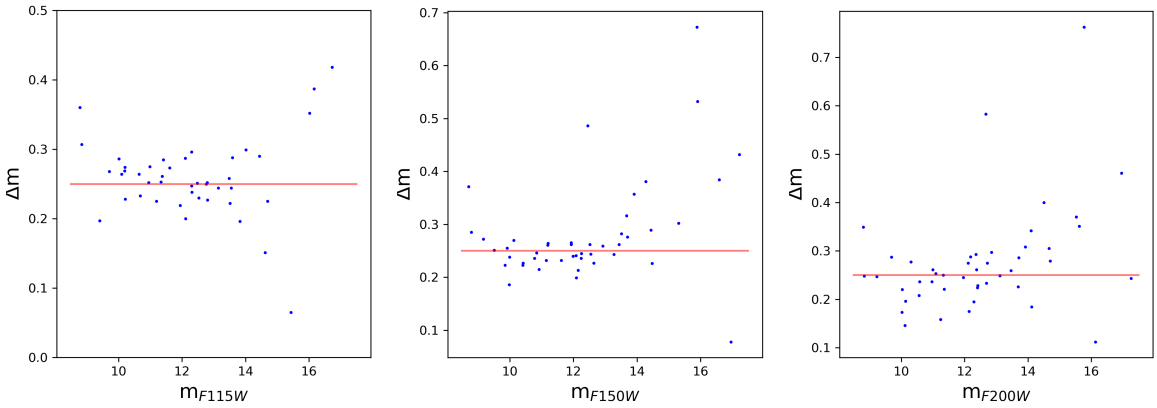

Figure B.6: delta m vs apparent magnitude from allstar for foreground stars in the field of **RXJ 2129**

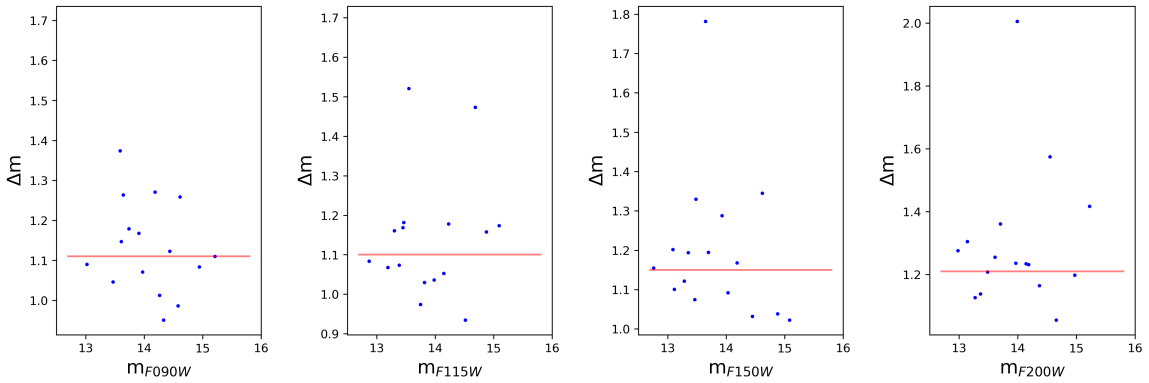

Figure B.7: delta m vs apparent magnitude from allstar for foreground stars in the field of **Abell 370**

where A_λ is the galactic extinction, k_λ is the cosmological K-correction, ZP_{AB} is the zeropoint for AB magnitudes, and $ZP_{daophot}$ is the daophot zeropoint (25 by default). ZP_{AB} depends on the units of the image in question; RXJ 2129 images are in units of MJy/sr, while Abell 370 images have been converted into units of nJy (`BUNIT` in image header).

Galactic extinction for each galaxy cluster (extrapolated to our wavelengths) is retrieved from the NED database (Schlafly and Finkbeiner, 2011). A_λ and k_λ terms are listed in Table B.1 for both RXJ 2129 and Abell 370. In the initial photometry steps, we scaled each image by a factor of 1000 for ease of processing. The $2.5 \log (1000\,\mathrm{s})$ term in Equation B.3 corrects for scaling.

For images in units of MJy/sr, the zeropoint is given by:

$$ZP_{AB} = -6.10 - 2.5 \log (\texttt{PIXAR\_SR}[\mathrm{sr/px}])^1 \tag{B.3.3}$$

where `PIXAR_SR` is the keyword for pixel size found in the FITS header.

System	Filter	A_λ	K
RXJ 2129	F115W	0.0396	-0.137
	F150W	0.0257	-0.130
	F200W	0.0166	-0.370
Abell 370	F090W	0.0436	-0.068
	F115W	0.0250	-0.227
	F150W	0.0155	-0.198
	F200W	0.0109	-0.454

Table B.1: Galactic extinction and cosmological K-corrections for relevant JWST NIRCam filters

Magnitudes are converted to absolute magnitudes for comparisons between galaxies:

$$(m - M)_\lambda = 5 \log \frac{d_L}{10\mathrm{pc}} \tag{B.3.4}$$

This assumes the K-correction was applied previously. Otherwise, it must be applied here.

[1] https://jwst-docs.stsci.edu/jwst-near-infrared-camera/nircam-performance/nircam-absolute-flux-calibration-and-zeropoints

B.4 Marking objects on a coloured image with ds9

Pyraf uses *tvmark* to mark objects on an image. Making a colour image, however, is done entirely in ds9. Circles or other markers are added to an image in ds9 using "regions". A *.reg* file looks something like this:

```
physical;circle(100,1000,3) #color=magenta
physical;circle(342,2800,3) #color=magenta
```

Shape and colour can be adjusted, and coordinates are input in the form `circle(x coordinate, y coordinate, marker radius)`. Thickness cannot be adjusted, but you can make markers appear thicker by layering markers with varying radii (e.g. two circles with the same coordinates, one with radius 7 and the other 7.5).

Finally, a warning for first-time users working on small laptops; "scale parameters" is used to set the minimum and maximum pixel values on an input image. It is near the bottom of the dropdown menu for "scale". If you are working on a smaller laptop, like me, this option may be cut off your screen, and there is no scroll bar or zoom settings for the ds9 window. I recommend making colour images with a monitor (or lower your resolution if you want to be sneaky).

Bibliography

A. B. Alabi, D. A. Forbes, A. J. Romanowsky, J. P. Brodie, J. Strader, J. Janz, V. Pota, N. Pastorello, C. Usher, L. R. Spitler, C. Foster, Z. G. Jennings, A. Villaume, and S. Kartha. The SLUGGS survey: the mass distribution in early-type galaxies within five effective radii and beyond. *Monthly Notices of the Royal Astronomical Society*, 460(4):3838–3860, 05 2016. ISSN 0035-8711. doi: 10.1093/mnras/stw1213. URL `https://doi.org/10.1093/mnras/stw1213`.

I. Alonso Asensio, C. Dalla Vecchia, Y. M. Bahé, D. J. Barnes, and S. T. Kay. The intracluster light as a tracer of the total matter density distribution: a view from simulations. *Monthly Notices of the Royal Astronomical Society*, 494(2):1859–1864, 04 2020. ISSN 0035-8711. doi: 10.1093/mnras/staa861. URL `https://doi.org/10.1093/mnras/staa861`.

A. Alves-Brito, G. K. T. Hau, D. A. Forbes, L. R. Spitler, J. Strader, J. P. Brodie, and K. L. Rhode. Spectra of globular clusters in the Sombrero galaxy: evidence for spectroscopic metallicity bimodality. MNRAS, 417(3):1823–1838, Nov. 2011. doi: 10.1111/j.1365-2966.2011.19368.x.

J. A. Arnold, A. J. Romanowsky, J. P. Brodie, L. Chomiuk, L. R. Spitler, J. Strader, A. J. Benson, and D. A. Forbes. The Fossil Record of Two-phase Galaxy Assembly:

Kinematics and Metallicities in the Nearest S0 Galaxy. ApJ, 736(2):L26, Aug. 2011. doi: 10.1088/2041-8205/736/2/L26.

P. Barmby, J. P. Huchra, J. P. Brodie, D. A. Forbes, L. L. Schroder, and C. J. Grillmair. M31 Globular Clusters: Colors and Metallicities. AJ, 119(2):727–747, Feb. 2000. doi: 10.1086/301213.

J. M. Berkheimer, T. Carleton, R. A. Windhorst, W. C. Keel, B. W. Holwerda, M. Nonino, S. H. Cohen, R. A. Jansen, D. Coe, C. J. Conselice, S. P. Driver, B. L. Frye, N. A. Grogin, A. M. Koekemoer, R. A. Lucas, M. A. Marshall, N. Pirzkal, C. Robertson, A. Robotham, R. E. Ryan, B. M. Smith, J. Summers, S. Tompkins, C. N. A. Willmer, and H. Yan. JWST NIRCam Photometry: A Study of Globular Clusters Surrounding Bright Elliptical Galaxy VV 191a at z = 0.0513. ApJ, 964 (2):L29, Apr. 2024. doi: 10.3847/2041-8213/ad2688.

J. M. Berkheimer, R. A. Windhorst, W. E. Harris, A. M. Koekemoer, T. Carleton, S. H. Cohen, R. A. Jansen, D. Coe, J. Diego, C. J. Conselice, S. P. Driver, B. L. Frye, N. A. Grogin, K. Hartman, T. R. Hinrichs, B. W. Holwerda, P. S. Kamieneski, K. E. Keatley, W. C. Keel, R. A. Lucas, M. A. Marshall, M. Nonino, N. Pirzkal, M. Ricotti, C. D. Robertson, A. Robotham, J. Russell E. Ryan, J. Summers, C. N. A. Willmer, and H. Yan. Globular clusters in the galaxy cluster macs0416 at z = 0.397, 2025. URL `https://arxiv.org/abs/2508.03883`.

J. P. Blakeslee, J. L. Tonry, and M. R. Metzger. Globular clusters in 19 northern abell clusters. *The Astronomical Journal*, 114:482, Aug. 1997. ISSN 0004-6256. doi: 10.1086/118488. URL `http://dx.doi.org/10.1086/118488`.

A. Bonaca and A. M. Price-Whelan. Stellar streams in the gaia era, 2024. URL https://arxiv.org/abs/2405.19410.

A. Bressan, P. Marigo, L. Girardi, B. Salasnich, C. Dal Cero, S. Rubele, and A. Nanni. PARSEC: stellar tracks and isochrones with the PAdova and TRieste Stellar Evolution Code. MNRAS, 427(1):127–145, Nov. 2012. doi: 10.1111/j.1365-2966.2012.21948.x.

N. Caldwell and A. J. Romanowsky. Star Clusters in M31. VII. Global Kinematics and Metallicity Subpopulations of the Globular Clusters. ApJ, 824(1):42, June 2016. doi: 10.3847/0004-637X/824/1/42.

G. B. Caminha, P. Rosati, C. Grillo, G. Rosani, K. I. Caputi, M. Meneghetti, A. Mercurio, I. Balestra, P. Bergamini, A. Biviano, M. Nonino, K. Umetsu, E. Vanzella, M. Annunziatella, T. Broadhurst, C. Delgado-Correal, R. Demarco, A. M. Koekemoer, M. Lombardi, C. Maier, M. Verdugo, and A. Zitrin. Strong lensing models of eight clash clusters from extensive spectroscopy: Accurate total mass reconstructions in the cores. *Astronomy & Astrophysics*, 632:A36, Nov. 2019. ISSN 1432-0746. doi: 10.1051/0004-6361/201935454. URL http://dx.doi.org/10.1051/0004-6361/201935454.

G. B. Caminha, S. H. Suyu, C. Grillo, and P. Rosati. Galaxy cluster strong lensing cosmography: Cosmological constraints from a sample of regular galaxy clusters. *Astronomy & Astrophysics*, 657:A83, Jan. 2022. ISSN 1432-0746. doi: 10.1051/0004-6361/202141994. URL http://dx.doi.org/10.1051/0004-6361/202141994.

Y. Chen and O. Y. Gnedin. Formation of globular clusters in dwarf galaxies of the

local group. *Monthly Notices of the Royal Astronomical Society*, 522(4):5638–5653, May 2023a. ISSN 1365-2966. doi: 10.1093/mnras/stad1328. URL http://dx.doi.org/10.1093/mnras/stad1328.

Y. Chen and O. Y. Gnedin. Catalogue of model star clusters in the milky way and m31 galaxies. *Monthly Notices of the Royal Astronomical Society*, 527(2):3692–3708, 11 2023b. ISSN 0035-8711. doi: 10.1093/mnras/stad3345. URL https://doi.org/10.1093/mnras/stad3345.

N. Choksi, O. Y. Gnedin, and H. Li. Formation of globular cluster systems: from dwarf galaxies to giants. MNRAS, 480(2):2343–2356, Oct. 2018. doi: 10.1093/mnras/sty1952.

A. Chu, F. Sarron, F. Durret, and I. Márquez. Physical properties of more than one thousand brightest cluster galaxies detected in the canada-france-hawaii telescope legacy survey. *Astronomy & Astrophysics*, 666:A54, Oct. 2022. ISSN 1432-0746. doi: 10.1051/0004-6361/202243504. URL http://dx.doi.org/10.1051/0004-6361/202243504.

G. Desprez, J. Richard, M. Jauzac, J. Martinez, B. Siana, and B. Clément. Galaxy-galaxy lensing in the outskirts of CLASH clusters: constraints on local shear and testing mass-luminosity scaling relation. MNRAS, 479(2):2630–2648, Sept. 2018. doi: 10.1093/mnras/sty1666.

J. M. Diego, K. B. Schmidt, T. Broadhurst, D. Lam, J. Vega-Ferrero, W. Zheng, S. Lee, T. Morishita, G. Bernstein, J. Lim, J. Silk, and H. Ford. A free-form lensing model of A370 revealing stellar mass dominated BCGs, in Hubble Frontier Fields images. MNRAS, 473(4):4279–4296, Feb. 2018. doi: 10.1093/mnras/stx2609.

V. Dornan and W. E. Harris. Investigating the M $_{GCS}$-M $_{h}$ Relation in the Most Massive Galaxies. ApJ, 950(2):179, June 2023. doi: 10.3847/1538-4357/accbc3.

V. Dornan and W. E. Harris. Major mergers mean major offset: Drivers of intrinsic scatter in the m_{GCS}–m_h scaling relation for massive elliptical galaxies. *The Astrophysical Journal*, 988(1):70, July 2025. ISSN 1538-4357. doi: 10.3847/1538-4357/ade05e. URL http://dx.doi.org/10.3847/1538-4357/ade05e.

K. Fahrion, M. Lyubenova, M. Hilker, G. van de Ven, J. Falcón-Barroso, R. Leaman, I. Martín-Navarro, A. Bittner, L. Coccato, E. M. Corsini, D. A. Gadotti, E. Iodice, R. M. McDermid, F. Pinna, M. Sarzi, S. Viaene, P. T. de Zeeuw, and L. Zhu. The Fornax 3D project: Globular clusters tracing kinematics and metallicities. A&A, 637:A26, May 2020. doi: 10.1051/0004-6361/202037685.

A. L. Faisst, R. R. Chary, G. Brammer, and S. Toft. What are those tiny things? a first study of compact star clusters in the smacs0723 field with jwst. *The Astrophysical Journal Letters*, 941(1):L11, Dec. 2022. ISSN 2041-8213. doi: 10.3847/2041-8213/aca1bf. URL http://dx.doi.org/10.3847/2041-8213/aca1bf.

D. A. Forbes, A. Alabi, A. J. Romanowsky, J. P. Brodie, J. Strader, C. Usher, and V. Pota. The sluggs survey: globular clusters and the dark matter content of early-type galaxies. *Monthly Notices of the Royal Astronomical Society: Letters*, 458(1):L44–L48, 02 2016. ISSN 1745-3925. doi: 10.1093/mnrasl/slw015. URL https://doi.org/10.1093/mnrasl/slw015.

D. A. Forbes, J. I. Read, M. Gieles, and M. L. M. Collins. Extending the globular cluster system–halo mass relation to the lowest galaxy masses. *Monthly Notices of*

the Royal Astronomical Society, 481(4):5592–5605, Sept. 2018. ISSN 1365-2966. doi: 10.1093/mnras/sty2584. URL http://dx.doi.org/10.1093/mnras/sty2584.

C. Foster, D. A. Forbes, R. N. Proctor, J. Strader, J. P. Brodie, and L. R. Spitler. Deriving Metallicities from the Integrated Spectra of Extragalactic Globular Clusters Using the Near-infrared Calcium Triplet. AJ, 139(4):1566–1578, Apr. 2010. doi: 10.1088/0004-6256/139/4/1566.

S. Giacintucci, M. Markevitch, R. Cassano, T. Venturi, T. E. Clarke, and G. Brunetti. Occurrence of Radio Minihalos in a Mass-limited Sample of Galaxy Clusters. ApJ, 841(2):71, June 2017. doi: 10.3847/1538-4357/aa7069.

M. Gieles, P. Padoan, C. Charbonnel, J. S. Vink, and L. Ramírez-Galeano. Globular cluster formation from inertial inflows: accreting extremely massive stars as the origin of abundance anomalies, 2025. URL https://arxiv.org/abs/2501.12138.

R. Gledhill, V. Strait, G. Desprez, G. Rihtaršič, M. Bradač, G. Brammer, C. J. Willott, N. Martis, M. Sawicki, G. Noirot, G. T. E. Sarrouh, and A. Muzzin. CANUCS: An Updated Mass and Magnification Model of A370 with JWST. ApJ, 973(2):77, Oct. 2024. doi: 10.3847/1538-4357/ad684a.

C. R. Harris, K. J. Millman, S. J. van der Walt, R. Gommers, P. Virtanen, D. Cournapeau, E. Wieser, J. Taylor, S. Berg, N. J. Smith, R. Kern, M. Picus, S. Hoyer, M. H. van Kerkwijk, M. Brett, A. Haldane, J. F. del Río, M. Wiebe, P. Peterson, P. Gérard-Marchant, K. Sheppard, T. Reddy, W. Weckesser, H. Abbasi, C. Gohlke, and T. E. Oliphant. Array programming with numpy. *Nature*, 585 (7825):357–362, Sept. 2020. ISSN 1476-4687. doi: 10.1038/s41586-020-2649-2. URL http://dx.doi.org/10.1038/s41586-020-2649-2.

W. Harris and J. Speagle. Photometric completeness modelled with neural networks. *The Astronomical Journal*, 168:38, 07 2024. doi: 10.3847/1538-3881/ad4a76.

W. E. Harris. A photometric survey of globular cluster systems in brightest cluster galaxies. *The Astrophysical Journal Supplement Series*, 265(1):9, Feb. 2023. ISSN 1538-4365. doi: 10.3847/1538-4365/acab5c. URL `http://dx.doi.org/10.3847/1538-4365/acab5c`.

W. E. Harris and R. E. Pudritz. Supergiant Molecular Clouds and the Formation of Globular Cluster Systems. ApJ, 429:177, July 1994. doi: 10.1086/174310.

W. E. Harris and M. Reina-Campos. JWST photometry of globular cluster populations in Abell 2744 at z = 0.3. MNRAS, 526(2):2696–2708, Dec. 2023. doi: 10.1093/mnras/stad2903.

W. E. Harris and M. Reina-Campos. JWST Photometry of Globular Clusters in A2744. II. Luminosity and Color Distributions. *Astrophys. J.*, 971(2):155, 2024. doi: 10.3847/1538-4357/ad583c.

W. E. Harris, W. Morningstar, O. Y. Gnedin, H. O'Halloran, J. P. Blakeslee, B. C. Whitmore, P. Côté, D. Geisler, E. W. Peng, J. Bailin, B. Rothberg, R. Cockcroft, and R. Barber DeGraaff. Globular Cluster Systems in Brightest Cluster Galaxies: A Near-universal Luminosity Function? ApJ, 797(2):128, Dec. 2014. doi: 10.1088/0004-637X/797/2/128.

W. E. Harris, G. L. Harris, and M. J. Hudson. Dark matter halos in galaxies and globular cluster populations. ii. metallicity and morphology. *The Astrophysical*

Journal, 806(1):36, June 2015. ISSN 1538-4357. doi: 10.1088/0004-637x/806/1/36. URL http://dx.doi.org/10.1088/0004-637X/806/1/36.

W. E. Harris, J. P. Blakeslee, and G. L. H. Harris. Galactic dark matter halos and globular cluster populations. iii. extension to extreme environments. *The Astrophysical Journal*, 836(1):67, Feb. 2017. ISSN 1538-4357. doi: 10.3847/1538-4357/836/1/67. URL http://dx.doi.org/10.3847/1538-4357/836/1/67.

W. E. Harris, M. Reina-Campos, A. M. Koekemoer, J. M. Berkheimer, T. Carleton, S. H. Cohen, B. L. Frye, T. R. Hinrichs, B. W. Holwerda, R. Honor, M. Ricotti, S. P. Willner, R. A. Windhorst, and H. Yan. Pearls: Globular clusters and ultra-compact dwarfs in the el gordo galaxies at z=0.87, 2025. URL https://arxiv.org/abs/2508.12862.

K. Hartman, W. Harris, J. Blakeslee, C.-P. Ma, and J. Greene. Comparing globular cluster system properties with host galaxy environment*. *The Astrophysical Journal*, 953:154, 08 2023. doi: 10.3847/1538-4357/ace340.

K. Hartman, W. E. Harris, and J. Kim. Sed fitting of globular clusters in ngc 4874: Masses and metallicities. *The Astrophysical Journal*, 990(1):65, 2025. doi: 10.3847/1538-4357/adf7ac.

M. J. Hudson and B. Robison. The correlation between the sizes of globular cluster systems and their host dark matter haloes. *Monthly Notices of the Royal Astronomical Society*, 477(3):3869–3885, Apr. 2018. ISSN 1365-2966. doi: 10.1093/mnras/sty844. URL http://dx.doi.org/10.1093/mnras/sty844.

J. D. Hunter. Matplotlib: A 2d graphics environment. *Computing in Science & Engineering*, 9(3):90–95, 2007. doi: 10.1109/MCSE.2007.55.

M. Jauzac, B. Klein, J.-P. Kneib, J. Richard, M. Rexroth, C. Schäfer, and A. Verdier. Galaxy cluster cores as seen with vlt/muse: New strong-lensing analyses of rx j2129.4 + 0009, ms 0451.6 - 0305, and macs j2129.4 - 0741. *Monthly Notices of the Royal Astronomical Society*, 508(1):1206–1226, Aug. 2021. ISSN 1365-2966. doi: 10.1093/mnras/stab2270. URL `http://dx.doi.org/10.1093/mnras/stab2270`.

Y. Jiménez-Teja, A. Gimenez-Alcazar, R. A. Dupke, P. Prado-Santos, J. M. Vilchez, N. O. L. de Oliveira, P. Dimauro, A. M. Koekemoer, P. Kelly, J. Hjorth, and W. Chen. First Joint MUSE, Hubble Space Telescope, and JWST Spectrophotometric Analysis of the Intracluster Light: The Case of the Relaxed Cluster RX J2129.7+0005. ApJ, 974(2):309, Oct. 2024. doi: 10.3847/1538-4357/ad701b.

W. A. Joye and E. Mandel. New Features of SAOImage DS9. In H. E. Payne, R. I. Jedrzejewski, and R. N. Hook, editors, *Astronomical Data Analysis Software and Systems XII*, volume 295 of *Astronomical Society of the Pacific Conference Series*, page 489, Jan. 2003.

R. Kale, T. Venturi, S. Giacintucci, D. Dallacasa, R. Cassano, G. Brunetti, V. Cuciti, G. Macario, and R. Athreya. The Extended GMRT Radio Halo Survey. II. Further results and analysis of the full sample. A&A, 579:A92, July 2015. doi: 10.1051/0004-6361/201525695.

S. S. Kartha, D. A. Forbes, L. R. Spitler, A. J. Romanowsky, J. A. Arnold, and

J. P. Brodie. The SLUGGS survey: the globular cluster systems of three early-type galaxies using wide-field imaging. MNRAS, 437(1):273–292, Jan. 2014. doi: 10.1093/mnras/stt1880.

A. Kassiola and I. Kovner. Elliptic Mass Distributions versus Elliptic Potentials in Gravitational Lenses. ApJ, 417:450, Nov. 1993. doi: 10.1086/173325.

B. W. Keller, J. M. D. Kruijssen, J. Pfeffer, M. Reina-Campos, N. Bastian, S. Trujillo-Gomez, M. E. Hughes, and R. A. Crain. Where did the globular clusters of the Milky Way form? Insights from the E-MOSAICS simulations. MNRAS, 495(4): 4248–4267, July 2020. doi: 10.1093/mnras/staa1439.

P. Kelly, T. J. Broadhurst, W. Chen, A. V. Filippenko, R. Foley, J. Hjorth, X. Huang, S. W. Jha, A. M. Koekemoer, M. Oguri, I. Perez-Fournon, J. Pierel, F. Poidevin, L.-G. Strolger, S. H. Suyu, T. L. Treu, and H. M. Williams. Imaging and Spectroscopy of Three Highly Magnified Images of a Supernova at z=1.5. JWST Proposal. Cycle 1, ID. #2767, Sept. 2022.

J. M. D. Kruijssen. On the fraction of star formation occurring in bound stellar clusters. MNRAS, 426(4):3008–3040, Nov. 2012. doi: 10.1111/j.1365-2966.2012.21923.x.

J. M. D. Kruijssen. The minimum metallicity of globular clusters and its physical origin - implications for the galaxy mass-metallicity relation and observations of proto-globular clusters at high redshift. MNRAS, 486(1):L20–L25, June 2019. doi: 10.1093/mnrasl/slz052.

J. M. D. Kruijssen. The formation of globular clusters, 2025. URL https://arxiv.org/abs/2501.16438.

J. M. D. Kruijssen, J. L. Pfeffer, M. Reina-Campos, R. A. Crain, and N. Bastian. The formation and assembly history of the milky way revealed by its globular cluster population. *Monthly Notices of the Royal Astronomical Society*, 486(3): 3180–3202, June 2018. ISSN 1365-2966. doi: 10.1093/mnras/sty1609. URL http://dx.doi.org/10.1093/mnras/sty1609.

J. M. D. Kruijssen, J. L. Pfeffer, R. A. Crain, and N. Bastian. The E-MOSAICS project: tracing galaxy formation and assembly with the age-metallicity distribution of globular clusters. MNRAS, 486(3):3134–3179, July 2019. doi: 10.1093/mnras/stz968.

D. J. Lagattuta, J. Richard, B. Clément, G. Mahler, V. Patrício, R. Pelló, G. Soucail, K. B. Schmidt, L. Wisotzki, J. Martinez, and D. Bina. Lens modelling Abell 370: crowning the final frontier field with MUSE. MNRAS, 469(4):3946–3964, Aug. 2017. doi: 10.1093/mnras/stx1079.

R. Leaman, D. A. VandenBerg, and J. T. Mendel. The bifurcated age-metallicity relation of Milky Way globular clusters and its implications for the accretion history of the galaxy. MNRAS, 436(1):122–135, Nov. 2013. doi: 10.1093/mnras/stt1540.

M. G. Lee, J. H. Bae, and I. S. Jang. Detection of intracluster globular clusters in the first jwst images of the gravitational lens cluster smacs j0723.3–7327 at z = 0.39. *The Astrophysical Journal Letters*, 940(1):L19, Nov. 2022. ISSN 2041-8213. doi: 10.3847/2041-8213/ac990b. URL http://dx.doi.org/10.3847/2041-8213/ac990b.

H. Li and O. Y. Gnedin. Star cluster formation in cosmological simulations - III. Dynamical and chemical evolution. MNRAS, 486(3):4030–4043, July 2019. doi: 10.1093/mnras/stz1114.

J. Ma, Z.-Y. Wu, T.-M. Zhang, S. Wang, Z. Fan, J.-H. Wu, H. Zou, C.-H. Du, X. Zhou, and Q.-R. Yuan. Metal abundance and kinematical properties of the M81 globular cluster system. *Research in Astronomy and Astrophysics*, 13(4):399–410, Apr. 2013. doi: 10.1088/1674-4527/13/4/003.

A. W. McConnachie, R. Ibata, N. Martin, A. M. N. Ferguson, M. Collins, S. Gwyn, M. Irwin, G. F. Lewis, A. D. Mackey, T. Davidge, V. Arias, A. Conn, P. Côté, D. Crnojevic, A. Huxor, J. Penarrubia, C. Spengler, N. Tanvir, D. Valls-Gabaud, A. Babul, P. Barmby, N. F. Bate, E. Bernard, S. Chapman, A. Dotter, W. Harris, B. McMonigal, J. Navarro, T. H. Puzia, R. M. Rich, G. Thomas, and L. M. Widrow. The large-scale structure of the halo of the andromeda galaxy. ii. hierarchical structure in the pan-andromeda archaeological survey. *The Astrophysical Journal*, 868(1):55, Nov. 2018. ISSN 1538-4357. doi: 10.3847/1538-4357/aae8e7. URL `http://dx.doi.org/10.3847/1538-4357/aae8e7`.

D. E. McLaughlin, W. E. Harris, and D. A. Hanes. The Spatial Structure of the M87 Globular Cluster System. ApJ, 422:486, Feb. 1994. doi: 10.1086/173744.

E. W. Peng, A. Jordán, P. Côté, J. P. Blakeslee, L. Ferrarese, S. Mei, M. J. West, D. Merritt, M. Milosavljević, and J. L. Tonry. The ACS Virgo Cluster Survey. IX. The Color Distributions of Globular Cluster Systems in Early-Type Galaxies. ApJ, 639(1):95–119, Mar. 2006. doi: 10.1086/498210.

J. Pfeffer, J. M. D. Kruijssen, R. A. Crain, and N. Bastian. The E-MOSAICS project:

simulating the formation and co-evolution of galaxies and their star cluster populations. MNRAS, 475(4):4309–4346, Apr. 2018. doi: 10.1093/mnras/stx3124.

J. Pfeffer, J. M. D. Kruijssen, N. Bastian, R. A. Crain, and S. Trujillo-Gomez. Globular cluster metallicity distributions in the e-mosaics simulations. *Monthly Notices of the Royal Astronomical Society*, 519(4):5384–5401, Jan. 2023. ISSN 1365-2966. doi: 10.1093/mnras/stad044. URL http://dx.doi.org/10.1093/mnras/stad044.

A. Pillepich, D. Nelson, L. Hernquist, V. Springel, R. Pakmor, P. Torrey, R. Weinberger, S. Genel, J. P. Naiman, F. Marinacci, and M. Vogelsberger. First results from the IllustrisTNG simulations: the stellar mass content of groups and clusters of galaxies. *Monthly Notices of the Royal Astronomical Society*, 475 (1):648–675, 12 2017. ISSN 0035-8711. doi: 10.1093/mnras/stx3112. URL https://doi.org/10.1093/mnras/stx3112.

Planck Collaboration, Ade, P. A. R., Aghanim, N., Arnaud, M., Ashdown, M., Aumont, J., Baccigalupi, C., Banday, A. J., Barreiro, R. B., Bartlett, J. G., Bartolo, N., Battaner, E., Battye, R., Benabed, K., Benoît, A., Benoit-Lévy, A., Bernard, J.-P., Bersanelli, M., Bielewicz, P., Bock, J. J., Bonaldi, A., Bonavera, L., Bond, J. R., Borrill, J., Bouchet, F. R., Boulanger, F., Bucher, M., Burigana, C., Butler, R. C., Calabrese, E., Cardoso, J.-F., Catalano, A., Challinor, A., Chamballu, A., Chary, R.-R., Chiang, H. C., Chluba, J., Christensen, P. R., Church, S., Clements, D. L., Colombi, S., Colombo, L. P. L., Combet, C., Coulais, A., Crill, B. P., Curto, A., Cuttaia, F., Danese, L., Davies, R. D., Davis, R. J., de Bernardis, P., de Rosa, A., de Zotti, G., Delabrouille, J., Désert, F.-X., Di Valentino, E., Dickinson, C., Diego, J. M., Dolag, K., Dole, H., Donzelli, S., Doré, O., Douspis, M., Ducout,

A., Dunkley, J., Dupac, X., Efstathiou, G., Elsner, F., Enßlin, T. A., Eriksen, H. K., Farhang, M., Fergusson, J., Finelli, F., Forni, O., Frailis, M., Fraisse, A. A., Franceschi, E., Frejsel, A., Galeotta, S., Galli, S., Ganga, K., Gauthier, C., Gerbino, M., Ghosh, T., Giard, M., Giraud-Héraud, Y., Giusarma, E., Gjerløw, E., González-Nuevo, J., Górski, K. M., Gratton, S., Gregorio, A., Gruppuso, A., Gudmundsson, J. E., Hamann, J., Hansen, F. K., Hanson, D., Harrison, D. L., Helou, G., Henrot-Versillé, S., Hernández-Monteagudo, C., Herranz, D., Hildebrandt, S. R., Hivon, E., Hobson, M., Holmes, W. A., Hornstrup, A., Hovest, W., Huang, Z., Huffenberger, K. M., Hurier, G., Jaffe, A. H., Jaffe, T. R., Jones, W. C., Juvela, M., Keihänen, E., Keskitalo, R., Kisner, T. S., Kneissl, R., Knoche, J., Knox, L., Kunz, M., Kurki-Suonio, H., Lagache, G., Lähteenmäki, A., Lamarre, J.-M., Lasenby, A., Lattanzi, M., Lawrence, C. R., Leahy, J. P., Leonardi, R., Lesgourgues, J., Levrier, F., Lewis, A., Liguori, M., Lilje, P. B., Linden-Vørnle, M., López-Caniego, M., Lubin, P. M., Macías-Pérez, J. F., Maggio, G., Maino, D., Mandolesi, N., Mangilli, A., Marchini, A., Maris, M., Martin, P. G., Martinelli, M., Martínez-González, E., Masi, S., Matarrese, S., McGehee, P., Meinhold, P. R., Melchiorri, A., Melin, J.-B., Mendes, L., Mennella, A., Migliaccio, M., Millea, M., Mitra, S., Miville-Deschênes, M.-A., Moneti, A., Montier, L., Morgante, G., Mortlock, D., Moss, A., Munshi, D., Murphy, J. A., Naselsky, P., Nati, F., Natoli, P., Netterfield, C. B., Nørgaard-Nielsen, H. U., Noviello, F., Novikov, D., Novikov, I., Oxborrow, C. A., Paci, F., Pagano, L., Pajot, F., Paladini, R., Paoletti, D., Partridge, B., Pasian, F., Patanchon, G., Pearson, T. J., Perdereau, O., Perotto, L., Perrotta, F., Pettorino, V., Piacentini, F., Piat, M., Pierpaoli, E., Pietrobon, D., Plaszczynski, S., Pointecouteau, E., Polenta, G., Popa, L., Pratt, G. W., Prézeau,

G., Prunet, S., Puget, J.-L., Rachen, J. P., Reach, W. T., Rebolo, R., Reinecke, M., Remazeilles, M., Renault, C., Renzi, A., Ristorcelli, I., Rocha, G., Rosset, C., Rossetti, M., Roudier, G., Rouillé d'Orfeuil, B., Rowan-Robinson, M., Rubiño-Martín, J. A., Rusholme, B., Said, N., Salvatelli, V., Salvati, L., Sandri, M., Santos, D., Savelainen, M., Savini, G., Scott, D., Seiffert, M. D., Serra, P., Shellard, E. P. S., Spencer, L. D., Spinelli, M., Stolyarov, V., Stompor, R., Sudiwala, R., Sunyaev, R., Sutton, D., Suur-Uski, A.-S., Sygnet, J.-F., Tauber, J. A., Terenzi, L., Toffolatti, L., Tomasi, M., Tristram, M., Trombetti, T., Tucci, M., Tuovinen, J., Türler, M., Umana, G., Valenziano, L., Valiviita, J., Van Tent, F., Vielva, P., Villa, F., Wade, L. A., Wandelt, B. D., Wehus, I. K., White, M., White, S. D. M., Wilkinson, A., Yvon, D., Zacchei, A., and Zonca, A. Planck 2015 results - xiii. cosmological parameters. *A&A*, 594:A13, 2016. doi: 10.1051/0004-6361/201525830. URL `https://doi.org/10.1051/0004-6361/201525830`.

M. Postman, D. Coe, N. Benítez, L. Bradley, T. Broadhurst, M. Donahue, H. Ford, O. Graur, G. Graves, S. Jouvel, A. Koekemoer, D. Lemze, E. Medezinski, A. Molino, L. Moustakas, S. Ogaz, A. Riess, S. Rodney, P. Rosati, K. Umetsu, W. Zheng, A. Zitrin, M. Bartelmann, R. Bouwens, N. Czakon, S. Golwala, O. Host, L. Infante, S. Jha, Y. Jimenez-Teja, D. Kelson, O. Lahav, R. Lazkoz, D. Maoz, C. McCully, P. Melchior, M. Meneghetti, J. Merten, J. Moustakas, M. Nonino, B. Patel, E. Regös, J. Sayers, S. Seitz, and A. Van der Wel. The Cluster Lensing and Supernova Survey with Hubble: An Overview. ApJS, 199(2):25, Apr. 2012. doi: 10.1088/0067-0049/199/2/25.

M. Reina-Campos and W. E. Harris. RESCUER: cosmological K-corrections for star clusters. MNRAS, 531(4):4099–4107, July 2024. doi: 10.1093/mnras/stae1414.

M. Reina-Campos, J. M. D. Kruijssen, J. L. Pfeffer, N. Bastian, and R. A. Crain. Formation histories of stars, clusters, and globular clusters in the e-mosaics simulations. *Monthly Notices of the Royal Astronomical Society*, 486 (4):5838–5852, May 2019. ISSN 1365-2966. doi: 10.1093/mnras/stz1236. URL http://dx.doi.org/10.1093/mnras/stz1236.

M. Reina-Campos, B. W. Keller, J. M. D. Kruijssen, J. Gensior, S. Trujillo-Gomez, S. M. R. Jeffreson, J. L. Pfeffer, and A. Sills. Introducing emp-pathfinder: modelling the simultaneous formation and evolution of stellar clusters in their host galaxies. *Monthly Notices of the Royal Astronomical Society*, 517(3):3144–3180, July 2022. ISSN 1365-2966. doi: 10.1093/mnras/stac1934. URL http://dx.doi.org/10.1093/mnras/stac1934.

M. Reina-Campos, S. Trujillo-Gomez, A. J. Deason, J. M. D. Kruijssen, J. L. Pfeffer, R. A. Crain, N. Bastian, and M. E. Hughes. Radial distributions of globular clusters trace their host dark matter halo: insights from the E-MOSAICS simulations. MNRAS, 513(3):3925–3945, July 2022. doi: 10.1093/mnras/stac1126.

J. Richard, J.-P. Kneib, M. Limousin, A. Edge, and E. Jullo. Abell 370 revisited: refurbished hubble imaging of the first strong lensing cluster. *Monthly Notices of the Royal Astronomical Society: Letters*, 402(1):L44–L48, 02 2010. ISSN 1745-3925. doi: 10.1111/j.1745-3933.2009.00796.x. URL https://doi.org/10.1111/j.1745-3933.2009.00796.x.

K. Rines, M. J. Geller, A. Diaferio, and M. J. Kurtz. Measuring the Ultimate Halo Mass of Galaxy Clusters: Redshifts and Mass Profiles from the Hectospec Cluster Survey (HeCS). ApJ, 767(1):15, Apr. 2013. doi: 10.1088/0004-637X/767/1/15.

E. F. Schlafly and D. P. Finkbeiner. Measuring Reddening with Sloan Digital Sky Survey Stellar Spectra and Recalibrating SFD. ApJ, 737(2):103, Aug. 2011. doi: 10.1088/0004-637X/737/2/103.

Science Software Branch at STScI. PyRAF: Python alternative for IRAF. Astrophysics Source Code Library, record ascl:1207.011, July 2012.

S. Seabold and J. Perktold. statsmodels: Econometric and statistical modeling with python. In *9th Python in Science Conference*, 2010.

A. Slizewski, X. Dufresne, K. Murdock, G. Eadie, R. Sanderson, A. Wetzel, and M. Jurić. Galactic mass estimates using dwarf galaxies as kinematic tracers. *The Astrophysical Journal*, 924(2):131, jan 2022. doi: 10.3847/1538-4357/ac390b. URL `https://dx.doi.org/10.3847/1538-4357/ac390b`.

P. B. Stetson. DAOPHOT: A Computer Program for Crowded-Field Stellar Photometry. PASP, 99:191, Mar. 1987. doi: 10.1086/131977.

J. Strader, M. A. Beasley, and J. P. Brodie. Globular Cluster Metallicity Subpopulations in NGC 4472. AJ, 133(5):2015–2019, May 2007. doi: 10.1086/512770.

V. Strait, M. Bradač, A. Hoag, K.-H. Huang, T. Treu, X. Wang, R. Amorin, M. Castellano, A. Fontana, B.-C. Lemaux, E. Merlin, K. B. Schmidt, T. Schrabback, A. Tomczack, M. Trenti, and B. Vulcani. Mass and light of abell 370: A strong and weak lensing analysis. *The Astrophysical Journal*, 868(2):129, Nov. 2018. ISSN 1538-4357. doi: 10.3847/1538-4357/aae834. URL `http://dx.doi.org/10.3847/1538-4357/aae834`.

D. Tody. The IRAF Data Reduction and Analysis System. In D. L. Crawford, editor, *Instrumentation in astronomy VI*, volume 627 of *Society of Photo-Optical Instrumentation Engineers (SPIE) Conference Series*, page 733, Jan. 1986. doi: 10.1117/12.968154.

D. Tody. IRAF in the Nineties. In R. J. Hanisch, R. J. V. Brissenden, and J. Barnes, editors, *Astronomical Data Analysis Software and Systems II*, volume 52 of *Astronomical Society of the Pacific Conference Series*, page 173, Jan. 1993.

S. Ueda, Y. Ichinohe, S. M. Molnar, K. Umetsu, and T. Kitayama. Gas Density Perturbations in the Cool Cores of CLASH Galaxy Clusters. ApJ, 892(2):100, Apr. 2020. doi: 10.3847/1538-4357/ab7bdc.

K. Umetsu, M. Sereno, S.-I. Tam, I. N. Chiu, Z. Fan, S. Ettori, D. Gruen, T. Okumura, E. Medezinski, M. Donahue, M. Meneghetti, B. Frye, A. Koekemoer, T. Broadhurst, A. Zitrin, I. Balestra, N. Benítez, Y. Higuchi, P. Melchior, A. Mercurio, J. Merten, A. Molino, M. Nonino, M. Postman, P. Rosati, J. Sayers, and S. Seitz. The Projected Dark and Baryonic Ellipsoidal Structure of 20 CLASH Galaxy Clusters. ApJ, 860(2):104, June 2018. doi: 10.3847/1538-4357/aac3d9.

E. Vanzella, A. Claeyssens, B. Welch, A. Adamo, D. Coe, J. M. Diego, G. Mahler, G. Khullar, V. Kokorev, M. Oguri, S. Ravindranath, L. J. Furtak, T. Y.-Y. Hsiao, Abdurro'uf, N. Mandelker, G. Brammer, L. D. Bradley, M. Bradač, C. J. Conselice, P. Dayal, M. Nonino, F. Andrade-Santos, R. A. Windhorst, N. Pirzkal, K. Sharon, S. E. de Mink, S. Fujimoto, A. Zitrin, J. J. Eldridge, and C. Norman. Jwst/nircam probes young star clusters in the reionization era sunrise arc. *The Astrophysical*

Journal, 945(1):53, Mar. 2023. ISSN 1538-4357. doi: 10.3847/1538-4357/acb59a. URL http://dx.doi.org/10.3847/1538-4357/acb59a.

M. L. Waskom. seaborn: statistical data visualization. *Journal of Open Source Software*, 6(60):3021, 2021. doi: 10.21105/joss.03021. URL https://doi.org/10.21105/joss.03021.

K. A. Woodley, W. E. Harris, T. H. Puzia, M. Gómez, G. L. H. Harris, and D. Geisler. The Ages, Metallicities, and Alpha Element Enhancements of Globular Clusters in the Elliptical NGC 5128: A Homogeneous Spectroscopic Study with Gemini/Gemini Multi-Object Spectrograph. ApJ, 708(2):1335–1356, Jan. 2010. doi: 10.1088/0004-637X/708/2/1335.

R. Zinn. The Globular Cluster System of the Galaxy. IV. The Halo and Disk Subsystems. ApJ, 293:424, June 1985. doi: 10.1086/163249.